

---

# PRIVATELY FINE-TUNED LLMs PRESERVE TEMPORAL DYNAMICS IN TABULAR DATA

---

**Lucas Rosenblatt**  
NYU\*  
New York, New York, USA  
lr2872@nyu.edu

**Peihan Liu**  
Columbia University\*  
New York, New York, USA  
pl2926@columbia.edu

**Ryan McKenna**  
Google Research  
Seattle, WA, USA  
mckennar@google.com

**Natalia Ponomareva**  
Google Research  
New York, New York, USA  
nponomareva@google.com

February 4, 2026

## ABSTRACT

Research on differentially private synthetic tabular data has largely focused on independent and identically distributed rows where each record corresponds to a unique individual. This perspective neglects the temporal complexity in longitudinal datasets, such as electronic health records, where a user contributes an entire (sub) table of sequential events. While practitioners might attempt to model such data by flattening user histories into high-dimensional vectors for use with standard marginal-based mechanisms, we demonstrate that this strategy is insufficient. Flattening fails to preserve temporal coherence even when it maintains valid marginal distributions. We introduce PATH, a novel generative framework that treats the full table as the unit of synthesis and leverages the autoregressive capabilities of privately fine-tuned large language models. Extensive evaluations show that PATH effectively captures long-range dependencies that traditional methods miss. Empirically, our method reduces the distributional distance to real trajectories by over 60% and reduces state transition errors by nearly 50% compared to leading marginal mechanisms while achieving similar marginal fidelity.

## 1 Introduction

Structured, tabular data is a fundamentally human method of organizing information. It is at least as old as c. 2500 BCE, when Mesopotamian scribes detailed agricultural management and ration lists in tables split by horizontal and vertical lines [31]. In the contemporary era, the ability to model such data has become a cornerstone of machine learning, with Transformer-based large language models (LLMs) demonstrating impressive fidelity in learning tabular distributions [3, 10].

However, modern tabular data is frequently sensitive, containing personal medical histories, financial transactions, or private behavioral traces. To mitigate privacy risks, differential privacy (DP) [9] has emerged as the gold standard for data release. A common approach to data release with DP is through the generation of *differentially private synthetic data* (DPSD) that is statistically similar to the original data. High quality DPSD preserves the statistical utility of the original private data while providing formal privacy guarantees. While there are powerful tabular DPSD methods based on marginal measurements, e.g. AIM [25] or GEM [21], these approaches predominantly rely on the assumption that the data consists of independent, identically distributed (i.i.d.) rows, where a single individual corresponds to a single row, and a full table represents a collection of many individuals.

---

\*Work done at Google as part of student researcher engagement.

This assumption breaks down in the presence of *longitudinal* or *temporal* tabular data. Consider electronic health records (EHR), such as the MIMIC dataset [13], where a patient’s health data is not a single static row, but a number of rows representing a trajectory of vital signs, lab results, and hospital events recorded over time. In this (and other) longitudinal settings, the unit of ownership is not a row, but an entire *table* (or sequence of events); i.e. each user owns a full table of data with a temporal component present between the rows in multiple columns, and the full dataset is a collection of such tables.

Were we to apply traditional marginal-based DPSD methods to this data, one could simply concatenate all user tables into a single table, using group privacy and assuming maximum number of rows per user or sampling or aggregating each user’s rows into a single row per user. This is, however, clearly undesirable if one wants to model temporal patterns in the data. Additionally, group-level privacy is too strong of a notion for this problem because it protects the privacy of every group of rows, even when the rows belong to different users. To preserve temporal trends, one would thus be forced to “flatten” all of the user trajectories into single, high-dimensional vectors that could be combined into one table. In Section 4 we define this flattening transformation formally; flattening can be catastrophic for utility, as we demonstrate later, in that it explodes the dimensionality of the domain and introduces artificial sparsity, making it difficult for marginal-based mechanisms to capture the complex, sequential dependencies inherent to the data.

To address this, we propose Private Autoregressive Trajectory Histories (PATH). Instead of synthesizing one table as a collection of rows, we seek to synthesize a full set of tables, each of which has the temporal component preserved. Here, the dataset is not a matrix of values, but is a collection of sub-matrices  $\mathbf{D} = (D^{(1)}, \dots, D^{(n)})$ , where each  $D^{(i)}$  represents the full history of user  $i$ . While we assume throughout this work that all  $D^{(i)}$  share a common schema, we note that our text-based framework could naturally accommodate a heterogeneous schema, where columns may vary between users. We leave a complete exploration of this alternative application to future work. We leverage the autoregressive capabilities of pre-trained LLMs (specifically, the Gemma 3 [37] family of models) to learn the distribution of these user-level tables directly. By fine-tuning LLMs with differential privacy (DP-SGD) [1], we can generate high-fidelity synthetic collections of tables that preserve intricate temporal dynamics, such as a varied pattern of heart rates across patients.

**Our contributions.** We formalize the synthesis of user-level tabular data and contribute the following:

- **Privacy unit as full table.** To the best of our knowledge, we are the first to consider a full table as the privacy unit for differentially private data synthesis and the first to identify a practical use case for this framing,

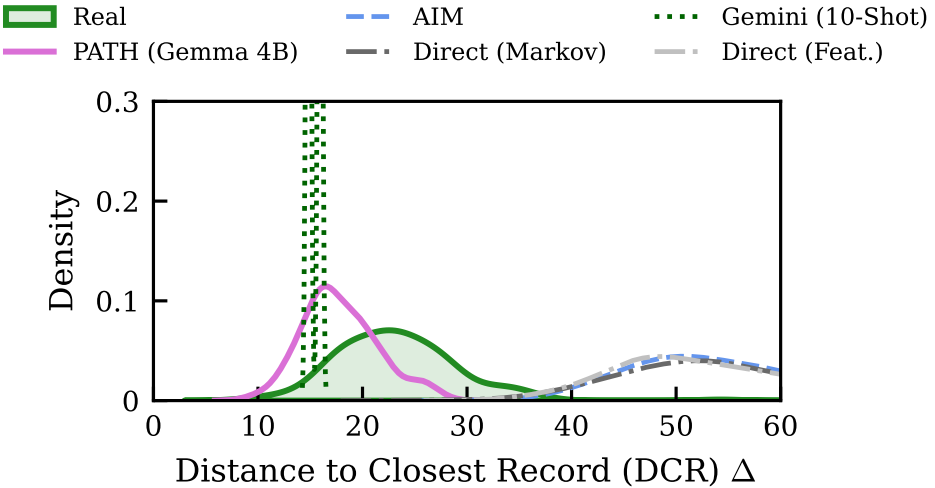


Figure 1: **Table-wise Distance to Closest Record (TDCR) Distribution Analysis ( $\varepsilon = 2.0$ ).** We visualize the distribution of distances from generated tables to their nearest neighbor in the real training set for MIMIC-IV Vital signs data using our Dynamic Time Warping-based metric. The green shaded area represents the “Real (Held-out)” baseline, showing the distances of real test tables to the training set; a high-fidelity synthetic method should produce a distribution that closely overlaps this baseline. Our proposed method, PATH (Gemma 4B), demonstrates superior overlap with the real data manifold compared to flattened marginal baselines (AIM, Direct) and non-private few-shot prompting (Gemini 2.5 Flash-Lite), which either mode-collapse (tight distribution on the left) or fail to capture the support (too far right).

specifically for preserving temporal trajectories where a user owns the entire table. This possibility was previously hinted at by [30] but lacked the application to temporal dynamics.

- **A novel framework for DP tabular data synthesis that preserves temporal trends.** Drawing inspiration from GReaT [3], we introduce a methodology for fine-tuning LLMs to generate structured, multi-row tabular data. We propose a novel two-stage generation process that begins with an autoregressive row-generation technique conditioning on previous context to preserve temporal dependencies (e.g., state transitions in vital signs) followed by a post-processing private selection step.
- **Novel metrics for table families.** Evaluating generative quality for families of tables requires more than standard row-wise metrics. We introduce *Table-wise Distance to Closest Record (TDCR)*, a metric adapted from Borisov et al. [3] to assess the *distributional* fidelity of generated user trajectories against real held-out data using Dynamic Time Warping (DTW). We additionally explore and report many other domain-specific time-series metrics (Section 3).
- **Extensive empirical evaluations.** We conduct extensive evaluations on a synthetic HMM dataset to control variable dependencies as well as on real-world MIMIC-IV vital signs [13] and NYC 311 service requests [27]. We demonstrate that traditional marginal-based methods scale poorly to the high dimensionality of flattened longitudinal data and fail to preserve temporal trends. Empirically, our method reduces the TDCR by over 50% compared to a state-of-the-art marginal baseline (AIM [25]), effectively capturing temporal dynamics that previous approaches miss.

## 2 Problem Formulation

Let  $\mathcal{U} = \{u_1, \dots, u_n\}$  be a set of  $n$  users. Each user  $u_i \in \mathcal{U}$  is associated with a single table  $D^{(i)}$  (e.g. trajectory of timesteps, recorded as rows), with  $d$  columns  $\mathcal{A} = \{A_1, \dots, A_d\}$ . Each attribute  $A_j$  is associated with a domain  $\mathcal{V}_j$ . Thus, a user  $u_i$ 's table  $D^{(i)}$  is an ordered sequence of  $T_i$  records (rows), or,

$$D^{(i)} = (\mathbf{x}_1^{(i)}, \mathbf{x}_2^{(i)}, \dots, \mathbf{x}_{T_i}^{(i)}), \quad (1)$$

where each record (row)  $\mathbf{x}_t^{(i)} = (v_{t,1}^{(i)}, \dots, v_{t,d}^{(i)})$  is a vector in the product space  $\mathcal{X} = \mathcal{V}_1 \times \dots \times \mathcal{V}_d$ . Crucially, the sequence length  $T_i$  is a random variable, and the sequence represents a temporal trajectory where the value of row  $\mathbf{x}_t^{(i)}$  depends on the history of previous rows  $\mathbf{x}_{<t}^{(i)} = (\mathbf{x}_1^{(i)}, \dots, \mathbf{x}_{t-1}^{(i)})$ .

**User-Level Differential Privacy.** We explicitly define the privacy unit as the full user table  $D^{(i)}$ , representing the complete history of a single user. Based on this unit, we adopt the add/remove definition of adjacency to ensure the entirety of an individual's trajectory is protected. Formally, two collections of user tables  $\mathbf{D}, \mathbf{D}'$  are **neighboring** ( $\mathbf{D} \simeq \mathbf{D}'$ ) if  $\mathbf{D}'$  can be obtained by adding or removing exactly one user  $u_i$  and their associated table  $D^{(i)}$ .

A mechanism  $\mathcal{M}$  satisfies  $(\varepsilon, \delta)$ -DP if for all neighboring  $\mathbf{D}, \mathbf{D}'$  and all measurable sets  $S \subseteq \text{Range}(\mathcal{M})$  it holds that,

$$\mathbb{P}[\mathcal{M}(\mathbf{D}) \in S] \leq e^\varepsilon \mathbb{P}[\mathcal{M}(\mathbf{D}') \in S] + \delta. \quad (2)$$

**Generative Goal.** Our objective is to learn a model  $f_\theta$  that approximates the density of the collection  $\mathbf{D}$ . During synthesis, the model must generate a synthetic collection  $\mathbf{D}^* = \{D^{(1)*}, \dots, D^{(n)*}\}$  that matches the source distribution, ensuring both the joint distribution of columns (intra-row correlations) and the temporal dependencies (inter-row correlations) match the source distribution.

## 3 Metrics

Evaluating the quality of synthetic longitudinal data requires assessing how realistic individual rows look (**marginal fidelity**), whether the *trajectories* from  $D^{(i)}$  maintain coherent temporal structures (**temporal integrity**), and if the collection  $\mathbf{D}^*$  covers the support of the real distribution without memorizing it (**distributional variety**).

To evaluate marginal fidelity, we examine the global distributions of individual columns by comparing their densities. To ensure temporal integrity, we measure the preservation of sequential dynamics through state transition matrices and Hidden Markov Model (HMM) likelihoods. Finally, to assess distributional variety and manifold coverage, we utilize embedding-based metrics such as MAUVE and our proposed Table-wise Distance to Closest Record (TDCR). See detailed formal definitions in Appendix Section D.

**Distributional Divergence (MAUVE).** To measure the gap between the manifolds of the real collection  $\mathbf{D}$  and the synthetic collection  $\mathbf{D}^*$ , we utilize MAUVE [28], which measures the information divergence between continuously embedded distributions (a score of 1.0 indicates perfect overlap). We map each variable-length table  $D^{(i)}$  to a fixed-length vector  $\mathbf{e}_i \in \mathbb{R}^k$  using Gecko embeddings [17], concatenating schema and mean row embeddings. Averaging row embeddings discards temporal sequencing information; thus, we utilize MAUVE to evaluate the overall distributional similarity of the tabular content rather than temporal fidelity (Section D.3).

**Table-wise Distance to Closest Record (TDCR).** Standard Euclidean distance is ill-defined for comparing tables of differing lengths. To evaluate fidelity, we must assess the *variety* of generated tables, ensuring the model covers the support of the real data rather than duplicating tables from a specific region. We introduce *Table-wise Distance to Closest Record* (TDCR). This metric extends the standard *Distance to Closest Record* (DCR) score [3] by utilizing Dynamic Time Warping (DTW) [15] to compute a robust distance  $\Delta(D^{(a)}, D^{(b)})$  between two user tables  $D^{(a)}$  and  $D^{(b)}$ . To compute DCR between two tables, we sum DTW distances of their corresponding attributes  $A_j$  and applying appropriate normalizations. This is crucial for longitudinal data, as it implicitly penalizes synthetic tables that fail to replicate the temporal shape and evolution of real trajectories, even if their aggregate marginals are correct. See Appendix Section D.2 for complete definition and Figure 7 for visual intuition.

Then, to evaluate the synthetic against real collections of tables, we compute the distance from every synthetic table  $D^{(i)*} \in \mathbf{D}^*$  to its nearest neighbor in the real training set. We perform the same operation for a held-out real test set to establish a baseline distribution of “real-to-real” distances. Finally, we quantify the similarity between the synthetic and test distance distributions using the Jensen-Shannon Distance (JSD). We privilege JSD over transport-based metrics like Wasserstein for this specific comparison because it robustly compares the shape of the distributions, effectively penalizing mode collapse where synthetic data might cluster in a high-density region without capturing the full variance of the manifold; see Section D.2 for more details.

**Temporal Integrity (State Transitions, HMM).** To assess the preservation of Markovian dynamics, we evaluate the *state* transition likelihoods, where state here is a quantile of the distribution. This metric is computed per feature, measuring the univariate conditional probability of a feature value at row  $j + 1$  given its value at row  $j$ , and does not capture cross-feature dependencies (e.g., how heart rate at  $t$  might affect blood pressure at  $t + 1$ ). We implement this by discretizing numerical features of all synthetic and real tables into quantiles to form transition matrices that estimate the probability of transitioning from one quantile to another. We distill the result into a single scalar by computing the Frobenius norm of the difference between the real and synthetic transition matrices for each feature, and report the average across all features (Section D.5).

For the case of “real” data that is completely synthetic, (where the ground truth data generation process is known (Section 6), we can evaluate long-range coherence by applying the true Gaussian HMM parameters to the private generated data [Jurafsky and Martin]. We compare log-likelihoods of held-out real trajectories to DP synthetic trajectories.

**Classifier Indistinguishability.** We posit that a marker of high-quality synthetic tables is that they are indistinguishable from real tables. Following the “classifier two-sample test” paradigm [23], we train classifiers (Logistic Regression, Random Forest, XGBoost) to discriminate between real and synthetic table embeddings (labeled binary, 0/1, and where worse predictive performance indicates better synthetic data). We utilize the same mean-pooled Gecko embeddings described in the MAUVE section, which capture the global semantic content of the table. Details on the classifier metric are in Section D.4.

**Categorical/Geospatial Metrics.** The NYC 311 dataset presents unique spatiotemporal and categorical challenges that require specialized evaluation beyond the previously discussed metric. For example, we assess temporal fidelity by extracting the “Hour of Day” from timestamps and computing the Wasserstein-1 distance between the real and synthetic diurnal distributions to ensure the daily rhythm of requests is preserved. To evaluate the geospatial features, we compare the joint distributions of latitude and longitude via hexbin density maps, allowing us to visually verify that the synthetic data respects the physical topology of the target distribution. Finally, to capture the semantic progression of user issues, we model complaint types as a Markov process. We construct a state transition matrix for the top- $k$  most frequent complaint categories, estimating the conditional probability  $P(\text{type}_t \mid \text{type}_{t-1})$ , and report the Frobenius norm of the difference between the real and synthetic matrices.

## 4 “Flattening” Longitudinal Data

To adapt traditional DP tabular synthesizers while attempting to retain the user-level trajectory structure, we apply a *flattening transformation*  $\Phi$  to map a table  $D^{(i)}$  of variable length  $T_i$  into a single fixed-width vector. Unfortunately, the distribution of trajectory lengths  $T_i$  could vary across users, forcing the use of extensive padding.

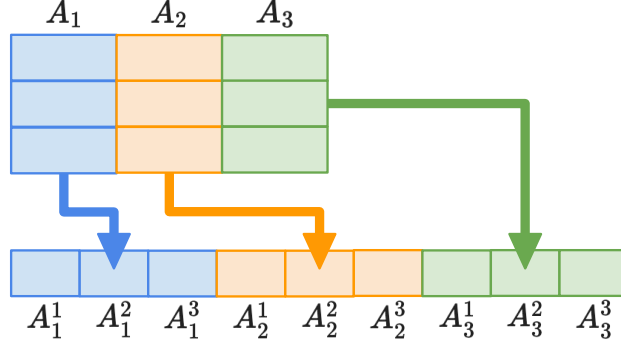


Figure 2: **The Flattening Transformation ( $\Phi$ ).** Visualizing how a user’s longitudinal history (left) is concatenated into a single high-dimensional vector (right). Each timestep becomes a distinct set of attributes (e.g.,  $A_1^1, A_1^2, \dots$ ), effectively multiplying the domain dimensionality by the sequence length  $L$ .

**Definition 1** (Flattening Transformation). Let  $\mathcal{V}'_j = \mathcal{V}_j \cup \{\text{NULL}\}$  be the augmented domain for a feature  $j$ . Let  $\mathbf{x}_\perp = (\text{NULL}, \dots, \text{NULL})$  be a padding vector of dimension  $d$ , and let  $L = \max_i T_i$  be the maximum sequence length across all users (or a truncation limit). The flattening transformation  $\Phi : D^{(i)} \rightarrow \mathbf{y}_i$  maps a variable-length table to a fixed-size sequence in  $\mathcal{Y} = (\mathcal{V}'_1 \times \dots \times \mathcal{V}'_d)^L$  by appending  $L - T_i$  padding vectors, or,

$$\mathbf{y}_i = (\mathbf{x}_1^{(i)}, \dots, \mathbf{x}_{T_i}^{(i)}, \underbrace{\mathbf{x}_\perp, \dots, \mathbf{x}_\perp}_{L-T_i}). \quad (3)$$

While applying  $\Phi$  enables the use of standard row-based DPSD mechanisms (e.g., AIM), it introduces a critical utility bottleneck rooted in the privacy budget. State-of-the-art tabular data synthesis methods measure low-degree marginals, as these are the least expensive, highest impact measurements in terms of privacy budget [21, 25, 33]. In this high-dimensional flattened space, these mechanisms measure low-order, local marginals (e.g., correlations between adjacent time steps  $\mathbf{x}_t$  and  $\mathbf{x}_{t+1}$ ). They do not, by default, measure all global dependencies; there are exponentially many of these, and it would be prohibitively expensive from both a computational and privacy budget perspective. We show an example in Appendix E (Proposition 1) of how, even if these methods preserve local step-wise plausibility, they could fail to maintain global consistency across the entire timeline. Consequently, if the true data contains distinct user “types” (e.g. healthy adults compared with adults requiring extensive medical visits) where the state at time  $t$  depends on the initial state at time 1, a locally-constrained mechanism would “mix” these trajectories, hallucinating spurious paths that are locally plausible but globally invalid. Additionally, we note that a trajectory that looks locally correct but is actually globally incoherent is a failure mode that is difficult to detect with standard marginal metrics, but is precisely what our TDCR metric is designed to penalize.

## 5 Proposing the PATH Generative Framework

We present PATH, a framework that captures the complex, time-dependent structure of user-level tabular data in an autoregressive manner. In contrast to flattening methods that attempt to model the joint distribution of a fixed-width vector, we treat the generation of a user’s trajectory as a conditional sequence generation task.

**Serialization.** Our deterministic serialization schema  $\Psi : D^{(i)} \rightarrow \mathbf{s}_i$ , maps a user’s table to a token sequence. As shown in Figure 3, the sequence begins with a schema definition, followed by the row-by-row encoding. We include row-delimiting tokens (e.g., [Row 1]) to encourage the model to distinguish between temporal steps.

The serialization format is designed to be invertible; any valid output string generated by the model can be parsed back into a structured table  $D^{(i)*}$ . We seek to encode the “history” of the user, implicitly capturing temporal dependencies via the language model’s context window rather than explicitly modeling the state-space.

**Data Construction and Privacy Unit.** Our framework strictly adheres to our *privacy unit*; to ensure that the DP guarantee protects the *entire* trajectory of a user rather than just isolated rows, we enforce that each user  $u_i$  contributes exactly one example to the gradient update per epoch.

To ensure robust autoregressive generation capabilities at any stage of the timeline, we employ a dynamic windowing strategy. For each user  $u_i$  at each epoch, we construct a single training example  $(\mathbf{c}_i, \mathbf{t}_i)$  by sampling a split point

```
Columns: charttime, heartrate, ...
[Row 1]: charttime is 2180-07-22 16:36:00,
heartrate is 83.0, ...
[Row 2]: charttime is 2180-09-22 16:43:00,
heartrate is 85.0, ...
```

Figure 3: The serialization format transforms longitudinal tables into a token sequence. The model learns to predict the next row conditioned on the schema and the history of previous rows.

$k \in [0, T_i - 1]$ . The model is provided with the context  $\mathbf{c}_i = \Psi(\mathbf{x}_{1:k}^{(i)})$  and trained to generate the target continuation  $\mathbf{t}_i = \Psi(\mathbf{x}_{k+1:T_i}^{(i)})$ . We then resample  $k$  independently at every epoch. This strategy allows the model to eventually learn from the full diversity of the user’s history and transition dynamics across the training process while maintaining a bounded sensitivity of 1 per user per step. We also want to train the model to iteratively generate a table *one row at a time*, which allows us to validate each row, and thus enforce coherence for the full generated table.

To ensure the model learns to generate trajectories at various stages of completion, we employ what we call a “density-based” sampling strategy. Rather than selecting the split point  $k$  uniformly, we sample  $k$  based on the empirical distribution of table lengths in the training set.<sup>2</sup> This prevents the model from being biased toward short contexts if the data contains a heavy tail of long trajectories. Specifically, with probability  $p_{\text{start}}$ , we select  $k = 0$  (generating the first row from scratch); otherwise, we sample  $k$  from the pool of all valid historical indices observed in the training corpus.

**Architecture and DP Fine-tuning.** We fine-tune models from the Gemma 3 family [36], specifically the 1B and 4B parameter variants (using the pre-trained checkpoints). We utilize Low-Rank Adaptation (LoRA) [12] with a rank of  $r = 128$ , which allows us to update a small fraction of parameters while freezing the pre-trained weights. This is particularly effective for DP training, as it reduces the dimensionality of the gradient updates that must be noised [16]. For more details on procedure and hyperparameters (which we fix for all datasets), see Section A.

**Inference, Parsing, and Private Selection** At inference time, we generate synthetic tables autoregressively, conditioning the generation of row  $\mathbf{x}_t$  on the schema and the history of previously generated rows  $\mathbf{x}_1, \dots, \mathbf{x}_{t-1}$ . Because DP fine-tuned models can yield malformed strings, we implement a robust parsing strategy to maximize data yield. For each generated step, we sequentially attempt to: (1) parse the output as structured key-value pairs (e.g., “col is val”); (2) fall back to parsing as comma-separated values matching the schema order if the first method fails; and (3) apply partial infilling to repair missing static identifiers (e.g., `subject_id`) by propagating values from the synthetic user’s existing history. If a row fails all validation checks, such as containing non-numeric values in numeric columns or invalid dates, the generation for that specific table is terminated early. This is fine, as we are able to “over-generate” table examples without consuming additional privacy budget. Finally, to ensure the final dataset  $\mathbf{D}^*$  has high utility, we employ a private selection strategy to post-process and filter a large, over-generated candidate pool [30]. See Appendix Section A for more details on the private selection procedure and parameters.

## 5.1 Baseline Approaches

**Real Data Subsampling (Reference).** To contextualize our metric scores, we evaluate a non-synthetic reference baseline consisting of real user tables uniformly subsampled from the training set (this is obviously not DP). We evaluate these subsamples at three distinct scales: 100, 1,000, and 10,000 unique tables. This comparison is important for interpreting distributional metrics like TDCR and MAUVE, as it establishes the “natural” variance and divergence one would expect simply due to finite sampling.

**Marginal-based Methods (on Flattened Data).** As discussed in Section 4, traditional DP tabular methods are designed to preserve relationships between columns of the data but do not generally preserve relationships between rows owned by the same user. To apply them to longitudinal data  $\mathbf{D}$ , we first apply the flattening transformation  $\Phi$  (Section 4). Note that for the flattened baselines we enforce a strict fixed-width window to ensure consistent marginal measurements. We filter the cohort to users with at least  $L$  timesteps (e.g.,  $L = 10$  for the MIMIC dataset) and truncate all trajectories to exactly this length. This results in a “wide” schema where each user contributes a single row with  $d \times L$  columns. Since marginal methods must discretize the domain, a single outlier can force an artificially wide bin that disproportionately assigns probability mass to implausible values. To correct for this, we heuristically clip all generated values to the [min, 99th percentile] range of the real private data. This is technically a violation of differential privacy (a DP version of this same approach would be strictly worse); we disregard this as it artificially strengthens the baselines, ensuring they are not penalized for susceptibility to outliers but rather evaluated on their core temporal modeling capacity.

<sup>2</sup>We assume this information to be public.

**Direct Mechanism.** We implemented a baseline following the *Select-Measure-Estimate* paradigm [26] with a fixed, heuristic selection strategy designed to capture temporal dynamics manually. To make this baseline exceptionally competitive (at the cost of using prior domain knowledge), we explicitly selected all 1-way marginals to capture feature distributions at each timestep and a specific set of 2-way marginals between adjacent time steps for every feature (e.g., measuring the joint distribution of  $(\text{heartrate}_t, \text{heartrate}_{t+1})$ ). In total, for a sequence length of  $L = 10$  and  $d = 9$  attributes (as is the case for MIMIC), this results in 90 1-way marginals and 81 temporal 2-way marginals. We used the Gaussian mechanism to measure these marginals with a uniform budget allocation and leveraged the Private-PGM package [26] to estimate the data distribution. This baseline effectively imposes a Markovian assumption, where the value for a feature at time  $t$  depends explicitly on its value at time  $t - 1$ .

We consider a second variant of the Direct Mechanism (referred to as “Direct (Across)”) where, in addition to the temporal correlations, we attempt to measure the relationship between different features at the same time step (e.g.,  $(\text{heartrate}_t, \text{resprate}_t)$ ). Since measuring all  $\binom{d}{2}$  attribute pairs across all  $L$  time steps creates a measurement set too large for tractable estimation (causing GPU memory exhaustion during the PGM step), we randomly subselect up to 80 of these intra-step marginals to include in the mechanism. This variant tests whether its more important to capture instantaneous correlations over Markovian steps.

**AIM.** We further evaluated the **AIM** algorithm [25], a leading workload-adaptive method. Unlike the Direct Mechanism, AIM automatically selects marginals using a greedy selection procedure that accounts for data, budget, and computational constraints [25, 30]. We provided AIM with the flattened dataset and allowed it to iteratively select the most informative marginals until the privacy budget was exhausted. This tests whether an automated selection metric can identify better temporal correlations than our manual heuristic in the high-dimensional flattened space, but we did not expect it to outperform the Direct mechanism, as Direct encodes knowledge about the temporal structure which AIM presumably needs to use some privacy budget to learn.

**Foundation Model Prompting (Non-Private).** To establish a utility upper bound for LLM-based generation, we evaluated the capabilities of Gemini 2.5 Flash-Lite (FL) without private fine-tuning [7]. We utilized In-Context Learning (ICL) with varying numbers of demonstration examples ( $k$ ). We used (1) Zero-shot ( $k = 0$ ) where the model is provided only with the schema and a natural language instruction to “generate a realistic tabular dataset for a patient,” (2) Few-shot ( $k \in \{1, 5, 10\}$ ), where we construct a prompt containing  $k$  real user tables randomly sampled from the training set, formatted using the same serialization scheme described in Section 5. The model is then tasked with generating a new, unique user table. See Appendix Section G for prompt text/structure.

## 6 Experimental Setup

**Data.** We evaluate our framework on three distinct datasets designed to test temporal coherence, generalization to unseen time periods, and ground-truth likelihoods. Details are provided in Appendix C.

**Vital signs subset of the MIMIC-IV dataset.** The privacy unit is a single patient (subject\_id). To focus on the most common temporal trajectories, we filter the cohort to include only patients with sequence lengths i.e. charttimes of  $4 \leq T \leq 50$ , resulting in a final dataset of 102,864 unique patient trajectories [13].

**NYC 311 calls.** To assess spatiotemporal fidelity and generalization, we use this data from October 1st, 2024, to August 1st, 2025 [27]. This time range post-dates the training cutoff of the pre-trained Gemma 3 models, ensuring performance reflects generalization rather than training data memorization. The privacy unit is a unique property (Borough-Block-Building (BBL)). This dataset contains 342,959 longitudinal service histories.

**Synthetically generated data (HMM).** As a controlled check for our methods and to measure the preservation of latent temporal states against a known ground truth, we generated a synthetic dataset using an HMM with multivariate Gaussian emissions [8] (see Appendix Section C). Unlike real data, where the true generative process is unknown, this allows us to rigorously evaluate the model’s ability to recover the exact transition probabilities and emission distributions governing the data.

## 7 Experimental Results

**The Utility Limits of Flattening.** Our results on the MIMIC-IV dataset, summarized in Table 1, empirically demonstrate the issues with flattening longitudinal data. When trajectories are concatenated into high-dimensional vectors, marginal-based methods struggle: at  $\varepsilon = 2.0$ , AIM achieves a TDCR of 0.736 compared to e.g. 0.289 for PATH (Gemma 4B). This gap indicates that AIM produces trajectories outside the true data manifold. Furthermore, flattening can dilute the privacy budget across the massive padded schema ( $d \times L$ ), degrading univariate utility. For example, AIM has a univariate marginal divergence of 9.71 (PATH has 3.30) – a failure mode visualized in Figure 4.

**Temporal Fidelity vs. Marginal Accuracy.** The Synthetic dataset, constructed via a ground-truth HMM, reveals a trade-off between column-wise independence and sequential logic. As shown in Table 10, though AIM achieves a superior univariate marginal divergence score (0.28 at  $\varepsilon = 10.0$ ) compared to PATH (Gemma 4B) (0.83), this marginal precision does not translate to preserved temporal dynamics. On the HMM Likelihood metric, which measures the probability of the generated sequences under the true latent process, PATH (both Gemma 1B and Gemma 4B) significantly outperforms AIM (50.99 vs. 319.43). While marginal methods accurately reproduce aggregate counts, they fail to capture the conditional probability  $P(\mathbf{x}_t | \mathbf{x}_{<t})$ . Conversely, PATH successfully learns the state transitions; this is qualitatively evident in the likelihood distributions shown in Figure 5 and quantitatively corroborated by the state transition divergence across all datasets (Tables 1-3), where Gemma 4B consistently yields lower Frobenius norms (e.g. 0.38 on MIMIC) compared to e.g. AIM (0.62).

**Distributional Manifolds and Generalization.** Beyond temporal metrics, we assess the overall distributional quality using MAUVE. On the complex, real-world datasets (MIMIC-IV and NYC 311), PATH (Gemma 4B) model consistently achieves the highest MAUVE scores among private methods. Specifically on MIMIC, PATH (Gemma 4B) ( $\varepsilon = 10.0$ ) reaches a MAUVE score of 0.651, surpassing the Direct Mechanism (0.596). We note that while marginal baselines outperform Gemma on the simpler Synthetic dataset (Table 2), this is likely due to the fact that the Synthetic data is very well behaved and thus admits the quantization necessary for the PGM based-baselines. We note that the non-private, few-shot in-context learning (on Gemini 2.5 FL) often underperformed our private fine-tuning; for instance, achieving a MAUVE score of only 0.269 on MIMIC. While few-shot prompting can copy local structure, it struggles to generalize the full distribution from a limited context window ( $k = 10$ ). PATH appears to internalize the distributional manifold over tables into the model weights, enabling the generation of a diverse table collection that better covers the real support.

**Model Scaling and Privacy Robustness.** Comparing the 1B and 4B parameter variants of Gemma for PATH demonstrates the importance of model scale, particularly at lower privacy budgets. While both models perform comparably at  $\varepsilon = 10.0$ , the 4B model exhibits significantly higher robustness as  $\varepsilon$  decreases. On MIMIC at  $\varepsilon = 0.5$ , the Gemma 1B model suffers a notable degradation in fidelity, with MAUVE scores dropping to 0.531 compared to 0.627 for the 4B model, and marginal divergence worsening from 3.00 (4B) to 3.93 (1B). We hypothesize that the larger model’s stronger pre-trained semantic priors provide a more stable initialization, allowing it to retain structural coherence even when the DP-SGD updates are dominated by noise. This trend holds for the NYC 311 dataset as well, where Gemma 4B consistently outperforms the 1B variant. Larger models are likely better equipped to handle complex schemas involving geospatial and high-dimensional categorical data.

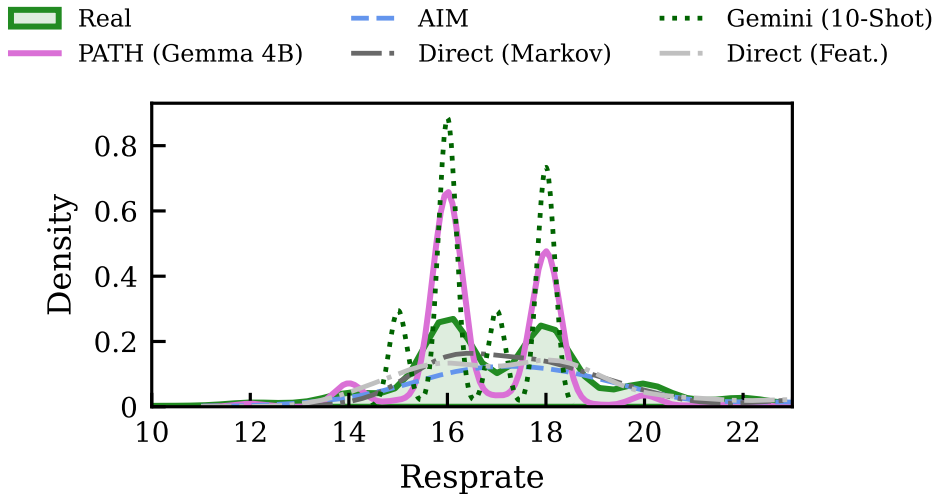


Figure 4: **Univariate Density Analysis (Respiratory Rate, MIMIC-IV).** We compare the marginal density of respiratory rate distributions across methods at  $\varepsilon = 2.0$ . While marginal-based baselines (AIM, Direct) achieve reasonable Wasserstein scores by broadly covering the support, they suffer from quantization smoothing and noise artifacts that obscure the data’s natural shape. In contrast, PATH closely tracks the sharp modal peaks and specific skew of the real distribution (shaded green), demonstrating that PATH can preserve fine-grained univariate trends.

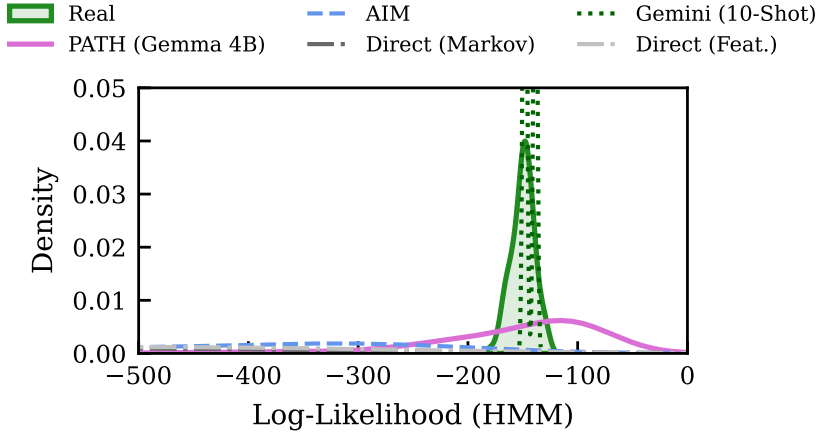


Figure 5: **HMM Log-Likelihood Distribution Analysis (Synthetic Dataset).** We evaluate long-range temporal coherence by scoring generated trajectories against the ground-truth HMM. The real data (shaded green) gives the variance in likelihood scores from our random process. The marginal-based baselines (AIM, Direct) produce a long tail of low-likelihood sequences (shifting left), indicating the generation of temporally incoherent trajectories that violate the underlying state transition logic. While non-private Gemini 2.5 FL (10-shot) produces a tight band of highly likely sequences, it fails to capture the full variance of the distribution (indicative of mode collapse). In contrast, PATH more successfully models the stochastic nature of the true process, producing a likelihood distribution closer to the support of the HMM data.

**Table 1** Performance comparison on the MIMIC dataset ( $\varepsilon \in \{2.0, 10.0\}$ ), evaluating privately fine-tuned LLMs against flattened marginal baselines. We include non-private Gemini 2.5 (10-shot or 10s) and Real Data subsamples as reference (upper bound) baselines. The results demonstrate that our autoregressive approach significantly outperforms marginal methods on temporal fidelity (State Trans.) and manifold coverage (MAUVE, TDCR) while also achieving superior marginal divergence. Notably, private fine-tuning achieves better distributional alignment than 10-shot prompting of the larger, non-private Gemini 2.5 Flash-Lite model. We follow the Olympic convention: gold represents the best metric values, silver the second best, and bronze third.

$\varepsilon$	Method	MAUVE ( $\uparrow$ )	TDCR (JSD $\downarrow$ )	Marginal Div. (Avg Wass. $\downarrow$ )	State Trans. (Avg Frob. $\downarrow$ )
2	AIM	0.564	0.7359	9.7080	0.7412
	DIRECT (Acr.)	0.493	0.7981	8.5031	0.6910
	DIRECT (Mark.)	0.573	0.7960	8.5788	0.5640
	PATH (1B)	0.596	0.4315	2.9174	0.3633
	PATH (4B)	0.661	0.2886	3.2980	0.3867
10	AIM	0.531	0.7349	5.7400	0.6243
	DIRECT (Acr.)	0.497	0.7665	8.3101	0.7076
	DIRECT (Indep)	0.596	0.7791	8.4024	0.5497
	PATH (1B)	0.552	0.3001	2.6486	0.4454
	PATH (4B)	0.651	0.3784	3.4125	0.3747
$\infty$	Gemini 2.5 FL (10s)	0.269	0.7894	5.9262	1.2283
	REAL (10k)	0.848	0.2322	0.3345	0.0161

**Table 2** Performance comparison on the HMM dataset ( $\varepsilon \in \{2.0, 10.0\}$ ). Our PATH (Gemma 4B) model achieves superior performance on temporal coherence metrics (HMM Likelihood, State Trans.) and distributional variety (TDCR).

$\varepsilon$	Method	MAUVE ( $\uparrow$ )	HMM Likelihood (Wass. $\downarrow$ )	TDCR (JSD $\downarrow$ )	Marginal Div. (Avg Wass. $\downarrow$ )	State Trans. (Avg Frob. $\downarrow$ )
2	AIM	0.655	374.47	0.6352	0.4260	0.5204
	DIRECT (Acr.)	0.763	696.55	0.7384	1.5437	0.6014
	DIRECT (Indep)	0.701	754.96	0.8059	1.8809	0.5953
	PATH (1B)	0.307	334.46	0.8073	3.0628	1.0329
	PATH (4B)	0.612	57.97	0.4150	0.9494	0.4363
10	AIM	0.705	319.43	0.5367	0.2757	0.4791
	DIRECT (Acr.)	0.704	409.11	0.6560	0.6496	0.5331
	DIRECT (Indep)	0.710	653.24	0.6748	0.9022	0.4558
	PATH (1B)	0.359	184.90	0.5402	2.5169	0.7138
	PATH (4B)	0.690	50.99	0.3966	0.8250	0.4217
$\infty$	Gemini 2.5 FL (10s)	0.268	9.02	0.5564	0.5596	0.6595
	REAL (10k)	0.856	0.33	0.1778	0.0325	0.0096

**Table 3** Performance comparison on the NYC 311 dataset ( $\varepsilon \in \{2.0, 10.0\}$ ). The PATH (Gemma 4B) model has high distributional fidelity (MAUVE) and temporal accuracy (Temporal Dist.) compared to the 1B model and the non-private baseline. Note that marginal baselines are excluded here as they failed to scale to the spatiotemporal schema of this dataset.

$\varepsilon$	Method	MAUVE (Gecko $\uparrow$ )	Classifier AUC (Ideal 0.5)	Temporal Dist. (Wass. $\downarrow$ )	Transition Div. (Frobenius $\downarrow$ )
2	PATH (1B)	0.311	0.955	1.400	0.605
	PATH (4B)	0.507	0.948	0.806	0.975
10	PATH (1B)	0.464	0.971	0.870	0.279
	PATH (4B)	0.634	0.948	0.870	0.405
$\infty$	Gemini 2.5 FL (10s)	0.074	1.000	2.537	-
	REAL (10k)	0.876	0.470	0.312	0.165

## 8 Related Work

See Section B for an extended discussion of related work.

**Marginal-based Mechanisms.** Mechanisms based on low-order marginals, such as Private-PGM [26] based methods like AIM [25], currently represent the state-of-the-art for i.i.d. tabular synthesis [30, 32, 6]. However, as we discussed, applying these mechanisms to longitudinal data requires flattening and extensive preprocessing (e.g., discretization), which can discard important features of the raw data.

**Transformer-based Synthesis.** Following GReaT [3], recent works serialize tabular data to fine-tune LLMs. To prevent the loss of structural coherence under DP-SGD [40], current methods often require complex two-stage training (learning syntax on public data, then distribution on private data) [2, 38]. While non-private methods like TabPFG [24] leverage strong tabular foundation models like TabPFN [11] for generation, they lack DP adaptations and are potentially ill-suited for modeling long-range temporal dependencies.

**Longitudinal DPSD.** Research on synthetic DP time-series data is limited. GAN-based approaches like DoppelGANger [19] and NetShare [39] often suffer significant utility loss under DP-SGD. Marginal adaptations like NetDPSyn [35] use PrivSyn [41] and focus on specific features (e.g., inter-arrival times); they assume event-level privacy rather than protecting full user trajectories, and thus target a different objective.

**Comparison of PATH with the above.** We operationalize the multi-table privacy unit suggested by Ponomareva et al. [30], and are the first to apply autoregressive LLMs. Unlike marginal methods, LLMs capture high-order dependencies [5] essential for longitudinal logic. In contrast to prior Transformer approaches to DPSD, PATH targets a different privacy objective (protecting user owned tables instead of rows) and achieves high fidelity with a single-stage training process and no preprocessing.

## 9 Conclusion

Considering our findings across medical, civic, and synthetic settings, we arrive at four primary conclusions. **First**, the “unit of synthesis” matters; treating a user’s trajectory as a single autoregressive sequence is a more efficient representation than flattening user histories. **Second**, there is a distinct dichotomy in utility; while marginal-based methods capture aggregate statistics well, LLMs dominate at capturing temporal dynamics and state transitions while also preserving these statistics, offering a “best of both worlds” solution. **Third**, private fine-tuning is more effective than in-context learning for distribution matching; few-shot prompting often leads to mode collapse, whereas fine-tuning captures population variety. **Fourth**, larger is better; Gemma 3 4B was better than its 1B variant at maintaining high temporal fidelity even under strict privacy guarantees.

In this work, we introduced Private Autoregressive Trajectory Histories (PATH), a generative framework that redefines the unit of differential privacy from the individual row to the entire user table. PATH leverages the autoregressive capabilities of privately fine-tuned LLMs, and addresses the fundamental limitations of flattening longitudinal data. Our extensive empirical analysis on the MIMIC-IV, NYC 311, and synthetic HMM datasets demonstrates that PATH yields superior fidelity across a suite of metrics when compared to state-of-the-art marginal-based baselines and prompting foundation models. These results establish that LLMs can serve as effective, privacy-preserving synthesizers in sequential tabular domains, enabling robust data sharing of sensitive temporal data.

## References

- [1] Abadi, M., Chu, A., Goodfellow, I., McMahan, H. B., Mironov, I., Talwar, K., and Zhang, L. (2016). Deep learning with differential privacy. In *Proceedings of the 2016 ACM SIGSAC Conference on Computer and Communications Security*, CCS’16, page 308–318. ACM.
- [2] Afonja, T., Wang, H.-P., Kerkouche, R., and Fritz, M. (2025). Dp-2stage: Adapting language models as differentially private tabular data generators.
- [3] Borisov, V., Seßler, K., Leemann, T., Pawelczyk, M., and Kasneci, G. (2022). Language models are realistic tabular data generators. *arXiv preprint arXiv:2210.06280*.
- [4] Bun, M., Gaboardi, M., Neunhoeffer, M., and Zhang, W. (2024). Continual release of differentially private synthetic data from longitudinal data collections. *Proceedings of the ACM on Management of Data*, 2(2):1–26.
- [5] Castellon, R., Gopal, A., Bloniarz, B., and Rosenberg, D. (2023). Dp-tbart: A transformer-based autoregressive model for differentially private tabular data generation.

[6] Chen, K., Li, X., Gong, C., Mckenna, R., and Wang, T. (2025). Benchmarking differentially private tabular data synthesis: [experiments, analysis]. *Proceedings of the ACM on Management of Data*, 3(6):1–25.

[7] Comanici, G., Bieber, E., Schaeckermann, M., Pasupat, I., Sachdeva, N., Dhillon, I., Blistein, M., Ram, O., Zhang, D., Rosen, E., et al. (2025). Gemini 2.5: Pushing the frontier with advanced reasoning, multimodality, long context, and next generation agentic capabilities. *arXiv preprint arXiv:2507.06261*.

[8] Durbin, R., Eddy, S. R., Krogh, A., and Mitchison, G. (1998). *Biological sequence analysis: probabilistic models of proteins and nucleic acids*. Cambridge university press.

[9] Dwork, C., McSherry, F., Nissim, K., and Smith, A. (2006). Calibrating noise to sensitivity in private data analysis. In *Theory of cryptography conference*, pages 265–284. Springer.

[10] Fang, X., Xu, W., Tan, F. A., Zhang, J., Hu, Z., Qi, Y., Nickleach, S., Socolinsky, D., Sengamedu, S., and Faloutsos, C. (2024). Large language models (llms) on tabular data: Prediction, generation, and understanding—a survey. *arXiv preprint arXiv:2402.17944*.

[11] Hollmann, N., Müller, S., Eggensperger, K., and Hutter, F. (2023). Tabpfn: A transformer that solves small tabular classification problems in a second.

[12] Hu, E. J., Shen, Y., Wallis, P., Allen-Zhu, Z., Li, Y., Wang, S., Wang, L., and Chen, W. (2021). Lora: Low-rank adaptation of large language models.

[13] Johnson, A., Bulgarelli, L., Pollard, T., Horng, S., Celi, L. A., and Mark, R. (2020). Mimic-iv. *PhysioNet*. Available online at: <https://physionet.org/content/mimiciv/1.0/> (accessed August 23, 2021), pages 49–55.

[Jurafsky and Martin] Jurafsky, D. and Martin, J. H. Speech and language processing: An introduction to natural language processing, computational linguistics, and speech recognition.

[15] Kruskal, J. B. (1983). An overview of sequence comparison: Time warps, string edits, and macromolecules. *SIAM review*, 25(2):201–237.

[16] Kurakin, A., Ponomareva, N., Syed, U., MacDermed, L., and Terzis, A. (2024). Harnessing large-language models to generate private synthetic text.

[17] Lee, J., Dai, Z., Ren, X., Chen, B., Cer, D., Cole, J. R., Hui, K., Boratko, M., Kapadia, R., Ding, W., et al. (2024). Gecko: Versatile text embeddings distilled from large language models. *arXiv preprint arXiv:2403.20327*.

[18] Li, X., Liu, D., Hashimoto, T. B., Inan, H. A., Kulkarni, J., Lee, Y.-T., and Guha Thakurta, A. (2022). When does differentially private learning not suffer in high dimensions? *Advances in Neural Information Processing Systems*, 35:28616–28630.

[19] Lin, Z., Jain, A., Wang, C., Fanti, G., and Sekar, V. (2020). Using gans for sharing networked time series data: Challenges, initial promise, and open questions. In *Proceedings of the ACM Internet Measurement Conference, IMC '20*, page 464–483. ACM.

[20] Liu, L., Pillutla, K., Welleck, S., Oh, S., Choi, Y., and Harchaoui, Z. (2021a). Divergence Frontiers for Generative Models: Sample Complexity, Quantization Effects, and Frontier Integrals. In *NeurIPS*.

[21] Liu, T., Vietri, G., and Wu, S. Z. (2021b). Iterative methods for private synthetic data: Unifying framework and new methods. *Advances in Neural Information Processing Systems*, 34:690–702.

[22] Livan, G., Novaes, M., and Vivo, P. (2018). Introduction to random matrices theory and practice. *Monograph Award*, 63(54):914.

[23] Lopez-Paz, D. and Oquab, M. (2016). Revisiting classifier two-sample tests. *arXiv preprint arXiv:1610.06545*.

[24] Ma, J., Dankar, A., Stein, G., Yu, G., and Caterini, A. (2024). Tabpfgan – tabular data generation with tabpfn.

[25] McKenna, R., Mullins, B., Sheldon, D., and Miklau, G. (2024). Aim: An adaptive and iterative mechanism for differentially private synthetic data.

[26] McKenna, R., Sheldon, D., and Miklau, G. (2019). Graphical-model based estimation and inference for differential privacy.

[27] NYC Dept. of Info Tech (2026). 311 Service Requests from 2010 to Present. Accessed: YYYY-MM-DD.

[28] Pillutla, K., Swayamdipta, S., Zellers, R., Thickstun, J., Welleck, S., Choi, Y., and Harchaoui, Z. (2021). Mauve: Measuring the gap between neural text and human text using divergence frontiers. In *NeurIPS*.

[29] Ponomareva, N., Hazimeh, H., Kurakin, A., Xu, Z., Denison, C., McMahan, H. B., Vassilvitskii, S., Chien, S., and Thakurta, A. G. (2023). How to dp-fy ml: A practical guide to machine learning with differential privacy. *Journal of Artificial Intelligence Research*, 77:1113–1201.

[30] Ponomareva, N., Xu, Z., McMahan, H. B., Kairouz, P., Rosenblatt, L., Cohen-Addad, V., Guzmán, C., McKenna, R., Andrew, G., Bie, A., Yu, D., Kurakin, A., Zadimoghaddam, M., Vassilvitskii, S., and Terzis, A. (2025). How to dp-fy your data: A practical guide to generating synthetic data with differential privacy.

[31] Robson, E. (2004). Accounting for change: the development of tabular book-keeping in early mesopotamia. *Creating economic order: Record-keeping, standardization, and the development of accounting in the Ancient Near East*, pages 107–144.

[32] Rosenblatt, L., Herman, B., Holovenko, A., Lee, W., Loftus, J., McKinnie, E., Rumezhak, T., Stadnik, A., Howe, B., and Stoyanovich, J. (2024). Epistemic parity: Reproducibility as an evaluation metric for differential privacy. *ACM SIGMOD Record*, 53(1):65–74.

[33] Rosenblatt, L., Lut, Y., Turok, E., Medina, M. A., and Cummings, R. (2025). Differential privacy under class imbalance: Methods and empirical insights. In *Forty-second International Conference on Machine Learning*.

[34] Song, S., Steinke, T., Thakkar, O., and Thakurta, A. (2021). Evading the curse of dimensionality in unconstrained private glms. In *International Conference on Artificial Intelligence and Statistics*, pages 2638–2646. PMLR.

[35] Sun, D., Chen, J. Q., Gong, C., Wang, T., and Li, Z. (2024). Netdpsyn: Synthesizing network traces under differential privacy.

[36] Team, G., Kamath, A., Ferret, J., Pathak, S., Vieillard, N., Merhej, R., Perrin, S., Matejovicova, T., Ramé, A., Rivière, M., et al. (2025). Gemma 3 technical report. *arXiv preprint arXiv:2503.19786*.

[37] Team, G., Mesnard, T., Hardin, C., Dadashi, R., Bhupatiraju, S., Pathak, S., Sifre, L., Rivière, M., Kale, M. S., Love, J., Tafti, P., Huszenot, L., Sessa, P. G., Chowdhery, A., Roberts, A., Barua, A., Botev, A., Castro-Ros, A., Slone, A., Héliou, A., Tacchetti, A., Bulanova, A., Paterson, A., Tsai, B., Shahriari, B., Lan, C. L., Choquette-Choo, C. A., Crepy, C., Cer, D., Ippolito, D., Reid, D., Buchatskaya, E., Ni, E., Noland, E., Yan, G., Tucker, G., Muraru, G.-C., Rozhdestvenskiy, G., Michalewski, H., Tenney, I., Grishchenko, I., Austin, J., Keeling, J., Labanowski, J., Lespiau, J.-B., Stanway, J., Brennan, J., Chen, J., Ferret, J., Chiu, J., Mao-Jones, J., Lee, K., Yu, K., Millican, K., Sjoesund, L. L., Lee, L., Dixon, L., Reid, M., Mikuła, M., Wirth, M., Sharman, M., Chinaev, N., Thain, N., Bachem, O., Chang, O., Wahltinez, O., Bailey, P., Michel, P., Yotov, P., Chaabouni, R., Comanescu, R., Jana, R., Anil, R., McIlroy, R., Liu, R., Mullins, R., Smith, S. L., Borgeaud, S., Girgin, S., Douglas, S., Pandya, S., Shakeri, S., De, S., Klimenko, T., Hennigan, T., Feinberg, V., Stokowiec, W., hui Chen, Y., Ahmed, Z., Gong, Z., Warkentin, T., Peran, L., Giang, M., Farabet, C., Vinyals, O., Dean, J., Kavukcuoglu, K., Hassabis, D., Ghahramani, Z., Eck, D., Barral, J., Pereira, F., Collins, E., Joulin, A., Fiedel, N., Senter, E., Andreev, A., and Kenealy, K. (2024). Gemma: Open models based on gemini research and technology.

[38] Tran, T. V. and Xiong, L. (2024). Differentially private tabular data synthesis using large language models.

[39] Yin, Y., Lin, Z., Jin, M., Fanti, G., and Sekar, V. (2022). Practical gan-based synthetic ip header trace generation using netshare. In *Proceedings of the ACM SIGCOMM 2022 Conference*, SIGCOMM '22, page 458–472, New York, NY, USA. Association for Computing Machinery.

[40] Yu, D., Naik, S., Backurs, A., Gopi, S., Inan, H. A., Kamath, G., Kulkarni, J., Lee, Y. T., Manoel, A., Wutschitz, L., et al. (2022). Differentially private fine-tuning of language models. In *International Conference on Learning Representations*.

[41] Zhang, Z., Wang, T., Li, N., Honorio, J., Backes, M., He, S., Chen, J., and Zhang, Y. (2020). Prvsyn: Differentially private data synthesis.

## A Architecture, Hyperparameters and Privacy Guarantees

We optimize the Gemma 1B and 4B models under PATH using DP-SGD [1]. We calibrate the noise multiplier  $\sigma$  to satisfy a *total* privacy budget  $\varepsilon_{total} \in \{0.5, 2.0, 4.0, 10.0\}$  with  $\delta = 1/n^2$ , where  $n$  is the number of unique subjects in the training set. We reserve a small portion of the privacy budget for the selection step (described below), such that  $\varepsilon_{total} = \varepsilon_{train} + \varepsilon_{select}$ .

We perform hyperparameter tuning on the learning rate and batch size using the Synthetic dataset, converging on a batch size of 256 and a peak learning rate of  $5 \times 10^{-4}$  with cosine decay. We utilize a fixed per-sample gradient clipping norm  $C = 0.01$ . These hyperparameter values are then used for all experiments on all datasets.

**DP Post-hoc Selection via Private Selection.** To ensure the final dataset  $\mathbf{D}^*$  has high utility, we employ a private selection strategy to post-process and filter a large, over-generated candidate pool [30]. To identify the most representative tables, we again map both real and synthetic data into a semantic vector space using the Gecko model [17]. We execute a differentially private voting mechanism where each private table casts votes for its  $k = 10$  nearest synthetic neighbors in this embedding space. The final dataset is composed of the candidates that receive the highest number of votes after the addition of privacy-preserving noise. For this selection step, we allocate a dedicated budget of  $\varepsilon_{select} = 1.0$ , scaling down to  $\varepsilon_{select} = 0.5$  and  $\varepsilon_{select} = 0.25$  for our tighter total budgets of  $\varepsilon = 2.0$  and  $\varepsilon = 0.5$ , respectively.

**Privacy Guarantees and Parameters.** Additionally, as suggested in [29], we provide a standardized report with important privacy specs from our experimentation.

## Privacy Guarantees and Parameters

1. **DP setting.** This work utilizes a *Central DP* model. The privacy guarantee applies to the release of the final synthetic dataset.
2. **Instantiating the DP Definition.**
  - (a) *Data accesses covered.* The privacy guarantee covers the training of the specific Generative Model (Gemma) and the subsequent Private Selection of synthetic tables. *Note on Hyperparameters:* Hyperparameter tuning (learning rate, batch size) was performed on a separate *Synthetic HMM* dataset and transferred to the real datasets. Therefore, the privacy budget reported is consumed entirely by the final training run and selection, without additional cost for tuning on the sensitive data.
  - (b) *What the final mechanism's output is.* The mechanism  $\mathcal{M}$  is defined as the composition of the DP-SGD fine-tuning, the autoregressive generation, and the Private Selection step. The output is the collection of synthetic tables  $\mathbf{D}^*$ . Generation and selection are post-processing of the DP-trained model and therefore do not incur additional privacy loss beyond the accounted training and selection mechanisms. While the model weights are differentially private, the primary release artifact is the synthetic data.
  - (c) *Unit of privacy.* User-level Privacy: the unit of protection is the full table  $D^{(i)}$  associated with a single user (e.g., a specific Patient ID in MIMIC or a specific Property BBL in NYC 311). This protects the entire longitudinal history of the user, not just individual rows.
  - (d) *Adjacency definition.* We utilize the Add-or-Remove definition of adjacency. Two datasets  $\mathbf{D}$  and  $\mathbf{D}'$  are neighboring if  $\mathbf{D}'$  can be obtained by adding or removing all records associated with exactly one user  $u_i$  from  $\mathbf{D}$ .
3. **Privacy accounting details.**
  - (a) *Type of accounting used.* We utilize *Privacy Loss Distribution (PLD)* accounting to compute tight bounds for the composition of subsampled Gaussian mechanisms.
  - (b) *Accounting assumptions.* The training process utilizes random shuffling (sampling without replacement), where each user contributes exactly one serialized sequence per epoch. For privacy accounting, we use PLD accounting specialized to shuffled (without-replacement) subsampling of the Gaussian mechanism with sampling rate  $q = B/n$  over the given number of epochs. The noise multiplier  $\sigma$  is calibrated to satisfy the target  $\varepsilon$  given the sampling rate  $q = B/n$  and number of epochs.
  - (c) *The formal DP statement.* The release satisfies  $(\varepsilon_{total}, \delta)$ -DP, where  $\delta = 1/n^2$  (e.g. approx  $10^{-10}$  for MIMIC). The total budget is composed of training and selection budgets:  $\varepsilon_{total} = \varepsilon_{train} + \varepsilon_{select}$ . Reported regimes are  $\varepsilon_{total} \in \{0.5, 2.0, 4.0, 10.0\}$ .
4. **Transparency and verifiability.** We will provide serialization logic and selection mechanism code upon acceptance.

## B Extended Related Work

**Marginal-based Mechanisms.** Mechanisms based on low-order marginal measurements currently represent the state-of-the-art for standard tabular data synthesis [30]. Popular approaches parameterize the distribution (e.g. the Private-PGM distributional model [26]), and cleverly update the distributional parameters by selecting and measuring a subset of column correlations. The most performant of these methods is AIM [25], which dominates recent benchmarks on independent and identically distributed (i.i.d.) tabular data [32, 6]. However, applying these mechanisms requires extensive preprocessing, including discretization, imputation, and outlier removal. Furthermore, by treating the data as purely numerical abstractions, these methods discard the semantic context inherent in column names and values. Additionally, some recent theoretical work has addressed the bounds of longitudinal release for streaming data [4], though these methods focus on continual aggregation rather than the synthesis of coherent individual trajectories.

**Transformer based models for DP Tabular data synthesis.** End-to-end methods utilizing Large Language Models (LLMs) for tabular synthesis have recently gained prominence. In the non-private setting, GReaT [3] serializes tabular data into textual strings (e.g., “Sex is Male, age is 50”) to fine-tune pre-trained LLMs. GReaT first creates a textual encoding of the tabular data (in the format “column\\_name is cell\\_value,”) [3] and then fine-tunes a pretrained LLM on such textual encodings. Column names are permuted during the encoding phase to avoid relying on pseudo-ordering of the column names and to allow sampling using any subset of column names. Adapting GReaT to the differentially private setting presents challenges; naive application of DP-SGD often results in the loss of structural coherence. To mitigate this, Afonja et al. [2] and [38] concurrently proposed a two-stage training paradigm: a first stage learns “format compliance” (syntax) on public data, followed by a second stage of DP fine-tuning on private data. Both works also introduce loss reweighting for formatting tokens (e.g., “is”, “,”) to further stabilize training.

A parallel line of work leverages TabPFN [11], a transformer pre-trained to perform supervised classification via in-context learning. TabPFGGen [24] is an energy-based model that harnesses TabPFN for (non-DP) data synthesis. TabPFGGen generates data via stochastic gradient Langevin dynamics (SGLD), iteratively refining noise into synthetic samples by maximizing the AUC of the in-context classifier. We exclude TabPFGGen from our evaluation for several reasons. First, the method requires designating a specific label column, limiting its generality. Second, the iterative energy-based update is ill-suited for capturing the long-range temporal dependencies central to our problem setting. Finally, no differentially private adaptation of TabPFGGen currently exists; given that TabPFN’s weights are immutable and fixed during pre-training, we hypothesize that the method would struggle to model private distributions that drift significantly from its pre-training prior.

**Longitudinal DPSD.** There is a noticeable lack of research activity on modeling multi-dimensional time series in differentially private settings, likely due to the difficulty of the problem. DoppelGANger [19] adapted GAN architectures by incorporating LSTMs to capture temporal dynamics. However, their experiments demonstrated that training with DP-SGD, even under moderate privacy budgets (e.g.,  $\epsilon = 10.5$ ), significantly degrades temporal correlations. Subsequent works, such as NetShare [39], reported similar utility losses with GAN-based approaches. This led to a paradigm shift toward marginal-based methods. For instance, NetDPSyn [35] adapted PrivSyn [41] to model network traces, capturing temporal dynamics by introducing inter-arrival times as an explicit feature and measuring marginals over these differences. These works typically define the privacy unit at the example (or event) level. In contrast, our framework adopts a stricter user-level definition, aiming to preserve the entire temporal trajectory of each synthetic user.

**Comparison of PATH with the above.** Our work distinguishes itself by operationalizing the multi-table privacy unit identified by Ponomareva et al. [30]. To the best of our knowledge, we are the first to leverage the autoregressive capabilities of LLMs to address the temporal modeling challenges inherent to this setting. While marginal-based methods excel at low-order statistics, recent literature suggests that LLMs are superior when capturing complex, high-order interactions [5]. Our results confirm that this capability is essential for modeling the conditional dependencies of longitudinal data. Furthermore, unlike prior transformer-based approaches that require complex two-stage training [2, 38], our framework achieves high fidelity with a single-stage standard next-token prediction loss. Finally, by learning directly from serialized tokens, we bypass the extensive preprocessing (e.g., discretization, outlier removal) required by marginal mechanisms, preserving the raw semantic richness of the data.

## C Data

### C.1 MIMIC IV

MIMIC vitalsigns data was preprocessed, first partitioning into users by *subject\_id* to create patient time-series data. We filtered out subjects who had more than 50 and fewer than 4 *charttime* (many patients, as is evidenced by Table 4, had fewer than 4 *charttime*, but we wanted patients with interesting temporal trajectories). Thus, we had a final cohort of 102,864 patients, reduced from the initial 198,131.

**Table 4** Comparison of MIMIC vital signs data before and after filtering.

Metric	Before Filtering			After Filtering			
	Record Counts	Unique ‘stay_id’	Unique ‘charttime’	Record Counts	Unique ‘stay_id’	Unique ‘charttime’	
count	198131	198131	198131	102864	102864	102864	
mean	7.90	2.06	7.90	10.58	2.43	10.58	
std	15.00	3.37	15.00	8.45	2.09	8.45	
min	1	1	1	4	1	4	
25%	2	2	2	5	1	5	
50%	4	4	4	7	2	7	
75%	8	8	8	13	3	13	
max	1144	1144	1144	50	30	50	

**Table 5** Sample table from the MIMIC-IV Vital-sign public sample data.

subject_id	stay_id	charttime	temperature	heartrate	resprate	o2sat	sbp	dbp	rhythm	pain
10014729	37887480	2125-03-19 13:22:00		124	24	100	93	65		
10014729	37887480	2125-03-19 18:28:00	98.9	106	18	100	115	70	Sinus Tachycardia	5
10014729	37887480	2125-03-19 13:07:00		128	18	100	132	96	Sinus Tachycardia	
10014729	37887480	2125-03-19 16:23:00	99.8	115	22	97	114	45	Sinus Tachycardia	0

### C.2 NYC 311 Calls/Requests

We use this data because (1) it has interesting geo-spatial *and* temporal trends for the model to pick up on, and (2) because it was released *after* the Gemma 3 class of model cutoff date (which was August 2024, according to Google). So, even though we can assume the Gemma models have been exposed to similar 311 call data (as its been public since 2010 on NYC Open Data), these specific calls are new, from a year distribution the model was not specifically trained on.

We use October 1st, 2024, through Aug 1st, 2025 of NYC 311 service requests (a dataset from NYC OpenData). This data was preprocessed, where “user-level” here is each unique “borough-block-building” code (a tax code that essentially identifies a single property with potentially multiple tenants). We removed columns that were redundant, empty, or had less precise information. We additionally filtered property-level such that properties (BBLs) with fewer than 2 total calls were excluded. Conversely, properties with more than 300 calls were removed. Thus, we went from an initial set of 381,066 unique properties to a final dataset of 118,510; then, each table is a time-series of 311 service requests for a specific property.

**Table 6** Sample of processed 311 data (column names changed for brevity).

key	created	closed	agency	complaint	descriptor	location_type	zip	address	resolution	bbl	latitude	longitude
62640682	2024-10-03 14:35:06	10/03/2024 02:53:31 PM	NYPD	Illegal Parking	Unauthorized Bus Layover	Street/Sidewalk	10004.00	10 PETER MINUIT PLAZA	(desc)	100030003.00	40.70	-74.01
62655723	2024-10-04 14:20:44	10/04/2024 02:38:27 PM	NYPD	Illegal Parking	Unauthorized Bus Layover	Street/Sidewalk	10004.00	10 PETER MINUIT PLAZA	(desc)	100030003.00	40.70	-74.01
62651993	2024-10-04 14:44:45	10/04/2024 03:04:03 PM	NYPD	Noise - Park	Loud Music/Party	Park/Playground	10004.00	10 PETER MINUIT PLAZA	(desc)	100030003.00	40.70	-74.01
62653125	2024-10-04 23:25:30	NaN	DHS	Homeless Person Assistance	NaN	Street/Sidewalk	10004.00	10 PETER MINUIT PLAZA	(desc)	100030003.00	40.70	-74.01
62672879	2024-10-06 13:04:18	10/06/2024 03:01:12 PM	DSNY	Vendor Enforcement	Food Vendor	Street	10004.00	10 PETER MINUIT PLAZA	NaN	100030003.00	40.70	-74.01

### C.3 Synthetic Data

It’s been known for quite some time that a Hidden Markov Model (HMM) is a good model for temporal dependencies in data [Jurafsky and Martin]. Thus, using a multivariate Gaussian emission space, we specify an HMM instance as  $(\mathcal{Q}, \mathcal{O}, \pi, A, B)$ . The finite set of  $N_s$  unobserved states is,

$$\mathcal{Q} = \{q_1, q_2, \dots, q_{N_s}\},$$

and the  $N_f$ -dimensional space of real-valued vectors from which observations are drawn is,

$$\mathcal{O} = \mathbb{R}^{N_f}.$$

We have initial state probabilities ( $\pi$ ), which is a vector of probabilities for the system's starting state at time  $t = 1$ , given,

$$\pi = [\pi_1, \pi_2, \dots, \pi_{N_s}], \quad \text{where } \pi_i = P(S_1 = q_i).$$

The dynamics of our model are governed by the transition probability matrix, denoted by  $A$ . This is an  $N_s \times N_s$  matrix where each element  $A_{ij}$  specifies the probability of transitioning from state  $q_i$  to state  $q_j$ . This captures the first-order Markov property of the sequence of latent states, or

$$A = \{A_{ij}\},$$

where  $A_{ij} = P(S_t = q_j | S_{t-1} = q_i)$ .

Finally, the connection between the latent states and the observable data is defined by the emission probability distributions, denoted by  $B$ . This is a set of  $N_s$  probability distributions, where each distribution  $b_i(\mathbf{o})$  gives the probability density of emitting the observation vector  $\mathbf{o} \in \mathcal{O}$  given that the system is in state  $q_i$ . In this model, each emission distribution is a multivariate normal distribution with a state-specific mean  $\mu_i$  and covariance matrix  $\Sigma_i$ .

$$B = \{b_1(\mathbf{o}), b_2(\mathbf{o}), \dots, b_{N_s}(\mathbf{o})\}$$

where  $b_i(\mathbf{o}) = p(\mathbf{O}_t = \mathbf{o} | S_t = q_i) \sim \mathcal{N}(\mu_i, \Sigma_i)$ .

So, to generate for each subject, a sequence of observations  $\mathbf{O}_1, \dots, \mathbf{O}_T$  of length  $T$  is drawn.

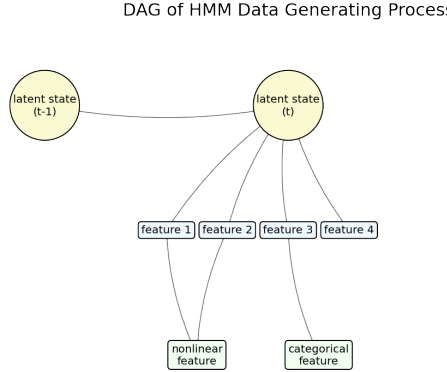


Figure 6: DAG for HMM.

**Table 7** Sample of Synthetic data

subject_id	timestep	Glomozole	Crirodex	Criphecor	Zolsidex	Zolphephine	Zolronide
10	0	-0.80	-2.10	-3.60	0.60	3.80	Low
10	1	2.70	-1.80	3.80	3.10	3.90	Very High
10	2	0.70	-2.70	2.70	3.40	8.00	High
10	3	0.60	-0.60	2.30	3.70	1.30	Medium
10	4	1.00	-1.50	4.10	2.40	2.00	Very High

## D Extended Metrics

### D.1 Univariate Marginal Distance

As a fundamental consistency check, we ensure the global marginal distributions of individual columns are preserved. We do this by aggregating the values of a specific feature  $c$  across all tables in the dataset into a single distribution, ignoring the temporal ordering. Let  $\mathcal{X}_c = \bigcup_i \{v_{t,c}^{(i)} \mid \mathbf{x}_t^{(i)} \in D^{(i)}\}$  be the multiset of all observed values for feature  $c$  in the real dataset, and let  $\mathcal{Y}_c$  be the corresponding multiset for the synthetic dataset.

We quantify the distance between these empirical distributions using the Wasserstein-1 distance.

**Definition 2** (Wasserstein-1 Distance). *For probability distributions  $\mu$  and  $\nu$  on  $\mathbb{R}$ , the 1-Wasserstein distance is:*

$$W_1(\mu, \nu) = \inf_{\gamma \in \Gamma(\mu, \nu)} \int_{\mathbb{R} \times \mathbb{R}} |x - y| d\gamma(x, y), \quad (4)$$

where  $\Gamma(\mu, \nu)$  denotes the set of all couplings (joint distributions) with marginals  $\mu$  and  $\nu$ .

In practice, we estimate this by computing the distance between the empirical distributions of  $\mathcal{X}_c$  and  $\mathcal{Y}_c$ . We privilege  $W_1$  over metrics like KL-Divergence because it respects the underlying geometry of the metric space (e.g., penalizing a generated heart rate of 180 bpm significantly more than 85 bpm if the true value is 80 bpm, whereas statistical metrics like TVD treat both errors identically).

### D.2 Table-wise Distance to Closest Record (TDCR)

Let the complete collection of real user tables be  $\mathbf{D}$ , which we split into disjoint training and test sets,  $\mathbf{D}_{\text{train}}$  and  $\mathbf{D}_{\text{test}}$ . Let  $\mathbf{D}^*$  be the collection of synthetic tables generated by our model. The first step is to formally define the distance  $\Delta(D^{(a)}, D^{(b)})$  between any two tables  $D^{(a)}, D^{(b)} \in \mathbf{D} \cup \mathbf{D}^*$ .

Recalling our problem formulation, a table  $D^{(i)}$  consists of  $d$  attributes  $\mathcal{A} = \{A_1, \dots, A_d\}$ . We define the trajectory for a specific attribute  $A_j$  in table  $D^{(i)}$  as the sequence of values  $\mathbf{v}_{\cdot,j}^{(i)} = (v_{1,j}^{(i)}, \dots, v_{T_i,j}^{(i)})$ .

The distance  $\Delta$  is a weighted sum of per-attribute time series distances,  $\delta_j$ . For a numerical attribute  $A_j$ , we define its distance as the normalized Dynamic Time Warping (DTW) distance:

$$\delta_j(\mathbf{v}_{\cdot,j}^{(a)}, \mathbf{v}_{\cdot,j}^{(b)}) = \frac{1}{|K|} \text{DTW}(\mathbf{v}_{\cdot,j}^{(a)}, \mathbf{v}_{\cdot,j}^{(b)}) \quad (5)$$

where  $K$  is the optimal warping path found by the DTW algorithm. This normalization accounts for varying sequence lengths  $T_a$  and  $T_b$ . The total inter-table distance is then the weighted  $L_1$  norm across all attributes:

$$\Delta(D^{(a)}, D^{(b)}) = \sum_{j=1}^d w_j \cdot \delta_j(\mathbf{v}_{\cdot,j}^{(a)}, \mathbf{v}_{\cdot,j}^{(b)}) \quad (6)$$

where weights  $w_j$  can be set to balance the contribution of each attribute. In our experiments, we set uniform weights  $w_j = 1$ .

Next, using this distance function, we compute the TDCR score for each table in our evaluation sets by finding its minimum distance to any table in the training set  $\mathbf{D}_{\text{train}}$ . For a synthetic table  $D^* \in \mathbf{D}^*$ , its score is:

$$\text{TDCR}(D^*) = \min_{D \in \mathbf{D}_{\text{train}}} \Delta(D^*, D) \quad (7)$$

And for a real test table  $D' \in \mathbf{D}_{\text{test}}$ , its benchmark score is:

$$\text{TDCR}(D') = \min_{D \in \mathbf{D}_{\text{train}}} \Delta(D', D) \quad (8)$$

This procedure yields two empirical distributions of minimum distances:  $P_{\text{synth}} = \{\text{TDCR}(D^*) \mid D^* \in \mathbf{D}^*\}$  and a benchmark distribution  $P_{\text{test}} = \{\text{TDCR}(D') \mid D' \in \mathbf{D}_{\text{test}}\}$ .

To quantify the fidelity of the synthetic data, we measure the divergence between these two distributions. Unlike transport-based metrics (e.g., Wasserstein) which focus on magnitude, we prioritize distributional shape. We discretize both  $P_{\text{synth}}$  and  $P_{\text{test}}$  into  $k$  histograms bins over their joint support, yielding discrete probability distributions  $P$  and  $Q$ . The final score is the Jensen-Shannon Distance (JSD), bounded in  $[0, 1]$ :

$$\text{TDCR}(\mathbf{D}^*, \mathbf{D}) = \sqrt{\frac{D_{KL}(P \parallel M) + D_{KL}(Q \parallel M)}{2}} \quad (9)$$

where  $M = \frac{1}{2}(P + Q)$  is the mixture distribution and  $D_{KL}$  is the Kullback-Leibler divergence. A lower JSD indicates that the privacy-utility trade-off mechanism has preserved the “distance-to-real” manifold of the held-out data.

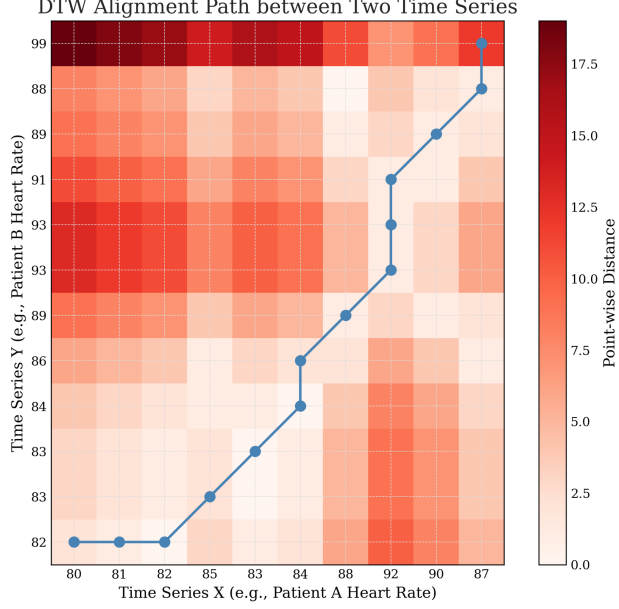


Figure 7: Dynamic Time Warping (DTW) alignment between two heart rate time series. The background heatmap represents the point-wise distance cost matrix, where darker red indicates a higher distance. The blue line traces the optimal warping path that minimizes the cumulative cost between Time Series X (Patient A:  $x = [80, 81, 82, 85, 83, 84, 88, 92, 90, 87]$ ) and Time Series Y (Patient B:  $y = [82, 83, 83, 84, 86, 89, 93, 93, 91, 89, 88, 99]$ ). The resulting Total DTW Distance for this example path is 25.0.

### D.3 MAUVE

Standard pairwise similarity approaches assume that comparing the average similarity of each table in set **A** directly to its closest neighbor in set **B** implicitly captures the closeness of the two families of tables. We adopt an alternative approach that measures the similarity of the distributions over the table embeddings using a divergence measure called MAUVE [20, 28]. We utilize the Gecko embedding model [17].

**Intuition.** First, we employ a lower-dimensional subspace transformation (via Gecko embeddings) to capture variance while mitigating computational cost and noise. Subsequently, k-means clustering is applied to partition the feature space into discrete clusters, providing a means to quantize the continuous data space into a finite set of representative bins. We use the cluster assignments to construct histograms, which give a discrete representation of the underlying data distributions. To handle data sparsity and zero-probability bins, we apply standard smoothing techniques.

The divergence curve is then generated by assessing the Kullback-Leibler (KL) divergence between the two distributions, and a mixture of both, across a range of mixing parameters. We distill this curve into a single scalar value, the MAUVE score, which corresponds to the area under the divergence curve. A score closer to 1 indicates high similarity. We normalize sample sizes between real and synthetic sets to ensure fair comparison.

**Formal Definition.** Calculating the MAUVE metric requires discretizing the continuous embedding space and measuring the KL-divergence between the two resulting distributions along a curve of their mixtures. Let  $\mathcal{P} = \{\mathbf{p}_1, \dots, \mathbf{p}_m\}$  and  $\mathcal{Q} = \{\mathbf{q}_1, \dots, \mathbf{q}_n\}$  be the sets of embeddings from the real and synthetic data, respectively, where each embedding vector lives in  $\mathbb{R}^d$ .

We combine the two sets into a single dataset and apply k-means clustering to partition the embedding space into  $k$  discrete clusters. This defines two multinomial probability distributions,  $P$  and  $Q$ , where for each cluster  $i \in \{1, \dots, k\}$ , the probabilities  $P(i)$  and  $Q(i)$  are the fractions of embeddings from  $\mathcal{P}$  and  $\mathcal{Q}$  assigned to that cluster.

We analyze their relationship by constructing a divergence curve. We define a mixture distribution  $R_\lambda = (1 - \lambda)P + \lambda Q$ , where  $\lambda \in [0, 1]$  is a mixing parameter. The divergence curve is a parametric plot of the KL divergences from the mixture to each original distribution. Specifically, the curve is traced by the points:

$$(D_{KL}(Q||R_\lambda), D_{KL}(P||R_\lambda)) \quad \forall \lambda \in [0, 1] \quad (10)$$

Here,  $D_{KL}(P||R_\lambda)$  quantifies Type I error (generating unrealistic samples), while  $D_{KL}(Q||R_\lambda)$  quantifies Type II error (mode collapse).

To bound the metric, we map the KL-divergence values to  $[0, 1]$  via an exponential scaling function,  $f(x) = e^{-c \cdot x}$ , where  $c$  is a scaling constant. The final MAUVE score is the area under this *scaled* parametric curve.

#### D.4 Classifier Discriminator

This metric employs a binary classifier to distinguish between “real” (original) tables and “synthetic” tables generated by the model. If the model produces high-quality synthetic data, the classifier should struggle to tell it apart from the real data (i.e., achieving an accuracy near 0.5 on a balanced set).

We utilize the Gecko embedding strategy described in Section 3, where each table  $D^{(i)}$  is converted to a vector  $\mathbf{v}_i$ . We construct a labeled dataset  $\mathcal{D}_{clf} = \{(\mathbf{v}, y) \mid \mathbf{v} \in \mathcal{P} \cup \mathcal{Q}\}$ , where  $y = 0$  for real tables and  $y = 1$  for synthetic tables. We split  $\mathcal{D}_{clf}$  into training (70%) and test (30%) sets. We train three classifiers: Logistic Regression, Random Forest, and XGBoost. We report the AUC-ROC on the held-out test set. We additionally inspect the separation of the predicted probability distributions  $P(\hat{y} = 1 \mid y = 0)$  and  $P(\hat{y} = 1 \mid y = 1)$  using Kernel Density Estimation plots to visualize the margin of separability.

#### D.5 State Transition Divergence

To evaluate the dynamics of how a system moves between different states, we discretize continuous features into a finite set of  $S$  states (using quantiles derived from the real data). From the sequence of states for all users, we estimate a state transition probability matrix,  $\mathbf{M} \in \mathbb{R}^{S \times S}$ , where an element  $M_{ij}$  represents the empirical probability of transitioning from state  $s_i$  to state  $s_j$ .

Let  $\mathbf{M}_R$  and  $\mathbf{M}_S$  be the transition matrices estimated from the real and synthetic datasets, respectively. The divergence between them is measured using the Frobenius norm of their difference:

$$D_{\text{trans}} = \|\mathbf{M}_R - \mathbf{M}_S\|_F = \sqrt{\sum_{i=1}^S \sum_{j=1}^S (M_{R,ij} - M_{S,ij})^2} \quad (11)$$

A divergence value closer to zero indicates that the fundamental dynamics of the state changes are well-captured in the synthetic data.

## E Limits of Flattening, Extended

In this section, we demonstrate the limitations of the flattening approach discussed in Section 4. When longitudinal data is flattened into high-dimensional vectors, the privacy cost of measuring global correlations typically becomes prohibitive, forcing marginal-based mechanisms to restrict their measurements to local neighborhoods (e.g., adjacent time steps). We show below that this restriction imposes a conditional independence structure on the synthetic distribution. Consequently, if the true data contains long-range dependencies, such as distinct user profiles that persist over time, a locally consistent mechanism will inevitably “mix” these profiles, assigning probability mass to spurious trajectories that are locally plausible but globally invalid.

**Definition 3** ( $k$ -Local Marginal Consistency). *Let  $P_\Phi$  be the true distribution over flattened vectors in  $\mathcal{Y}$ . A synthetic distribution  $P^*$  satisfies  $k$ -local marginal consistency with  $P_\Phi$  if for all time steps  $1 \leq t \leq L - k + 1$ , the marginal distribution on contiguous temporal windows matches the source:*

$$\mathbb{P}_{P^*}(\mathbf{x}_t, \dots, \mathbf{x}_{t+k-1}) = \mathbb{P}_{P_\Phi}(\mathbf{x}_t, \dots, \mathbf{x}_{t+k-1}). \quad (12)$$

Standard marginal-based approaches generate the distribution with Maximum Entropy among those satisfying the measured marginals [25]. We show that if a mechanism is restricted to  $k$ -local marginals (due to budget constraints preventing the measurement of global correlations), it *must* hallucinate invalid data for certain datasets.

**Proposition 1** (Spurious Trajectories in Local MaxEnt Distributions). *Let  $L = 3$  and  $k = 2$ . There exists a source distribution supported on a valid set of trajectories  $\mathcal{S} \subset \mathcal{Y}$ , such that the Maximum Entropy distribution  $P^*$  satisfying 2-local marginal consistency assigns non-zero probability to invalid trajectories  $\mathbf{y} \notin \mathcal{S}$ .*

*Proof.* Let the row domain be  $\{\alpha, \beta, \gamma\}$  with fixed trajectory length  $L = 3$ . We construct the source distribution as an equiprobable mixture of two user types: Type A, defined by  $\mathbf{y}_A = (\alpha, \gamma, \alpha)$ , and Type B, defined by  $\mathbf{y}_B = (\beta, \gamma, \beta)$ . The valid support is therefore  $\mathcal{S} = \{\mathbf{y}_A, \mathbf{y}_B\}$ . Examining the pairwise adjacent marginals, we observe that  $\mathbb{P}[\mathbf{x}_1, \mathbf{x}_2]$  is uniform on  $\{(\alpha, \gamma), (\beta, \gamma)\}$ , implying a deterministic transition, i.e.  $\mathbb{P}[\mathbf{x}_2 = \gamma \mid \mathbf{x}_1] = 1$ . Similarly,  $\mathbb{P}[\mathbf{x}_2, \mathbf{x}_3]$  is uniform on  $\{(\gamma, \alpha), (\gamma, \beta)\}$ , yielding  $\mathbb{P}[\mathbf{x}_3 = \alpha \mid \mathbf{x}_2 = \gamma] = 0.5$ . The Maximum Entropy distribution  $P^*$  consistent with these local marginals necessarily satisfies the conditional independence  $\mathbf{x}_1 \perp \mathbf{x}_3 \mid \mathbf{x}_2$  (i.e. a Markov chain structure). Under this independence, we compute the likelihood of the “mixed” trajectory  $\mathbf{z} = (\alpha, \gamma, \beta)$  as,

$$\mathbb{P}_{P^*}[\mathbf{z}] = \mathbb{P}[\mathbf{x}_1 = \alpha] \cdot \mathbb{P}[\mathbf{x}_2 = \gamma \mid \mathbf{x}_1 = \alpha] \cdot \mathbb{P}[\mathbf{x}_3 = \beta \mid \mathbf{x}_2 = \gamma] = 0.5 \cdot 1.0 \cdot 0.5 = 0.25. \quad (13)$$

Since  $\mathbf{z} \notin \mathcal{S}$ , we conclude that  $P^*$  assigns probability mass to spurious records.  $\square$

**Remark 1.** *Proposition 1 highlights that flattening fails to preserve long-range temporal dependencies (e.g.,  $T_1$  predicting  $T_3$ ) when the synthesizer relies on local dependency structures to save privacy budget. While global marginals could capture this, they are often too costly to measure in high dimensions. This motivates an alternate approach, one specifically designed to model sequential data with long-range dependencies.*

## F All Results

We include extensive summary and detail tables here with all our metrics, alongside an example of an NYC 311 set of plots in Section F.1. **Many additional plots are available upon request (excluded here for brevity of this document).**

**Table 8 Comprehensive Summary of Metrics on MIMIC-IV.** We report the performance of PATH (Gemma 1B/4B) against marginal baselines and non-private reference points across four privacy regimes. Beyond the results already reported in the main body of the paper, we observe a distinct degradation pattern in the marginal baselines: AIM’s marginal divergence explodes at  $\varepsilon = 0.5$  (18.48), whereas PATH remains remarkably stable ( $\approx 3.0$ ), suggesting the LLM’s pre-trained priors provide robustness when the privacy signal is weak. Additionally, comparing the “Real (100)” subsample to our synthetic results reveals that for distributional metrics like TDCR, our privately fine-tuned models ( $\approx 0.28 - 0.40$ ) are approaching the natural variance observed between small subsamples of real data ( $\approx 0.19$ ).

Method	MAUVE (Gecko $\uparrow$ )	HMM Likelihood (Wass. $\downarrow$ )	TDCR (Privacy) (JSD $\downarrow$ )	Marginal Div. (Avg Wass. $\downarrow$ )	State Trans. Div. (Avg Frobenius $\downarrow$ )
AIM (Clipped, $\varepsilon = 0.5$ )	0.587	-	0.8326	18.4848	0.9067
DIRECT (Across, Clipped, $\varepsilon = 0.5$ )	0.608	-	0.7937	12.8130	0.7607
DIRECT (Indep, Clipped, $\varepsilon = 0.5$ )	0.595	-	0.8218	12.2337	0.7299
Gemma 1B ( $\varepsilon = 0.5$ )	0.531	-	0.3470	3.9333	0.4819
Gemma 4B ( $\varepsilon = 0.5$ )	0.627	-	0.3376	3.0028	0.3817
AIM (Clipped, $\varepsilon = 2.0$ )	0.564	-	0.7359	9.7080	0.7412
DIRECT (Across, Clipped, $\varepsilon = 2.0$ )	0.493	-	0.7981	8.5031	0.6910
DIRECT (Indep, Clipped, $\varepsilon = 2.0$ )	0.573	-	0.7960	8.5788	0.5640
Gemma 1B ( $\varepsilon = 2.0$ )	0.596	-	0.4315	2.9174	0.3633
Gemma 4B ( $\varepsilon = 2.0$ )	0.661	-	0.2886	3.2980	0.3867
AIM (Clipped, $\varepsilon = 4.0$ )	0.501	-	0.7820	7.2091	0.6189
DIRECT (Across, Clipped, $\varepsilon = 4.0$ )	0.541	-	0.7573	8.2982	0.6722
DIRECT (Indep, Clipped, $\varepsilon = 4.0$ )	0.532	-	0.7615	8.0687	0.5746
Gemma 1B ( $\varepsilon = 4.0$ )	0.554	-	0.3365	3.4431	0.3855
Gemma 4B ( $\varepsilon = 4.0$ )	0.600	-	0.4112	4.0971	0.3816
AIM (Clipped, $\varepsilon = 10.0$ )	0.531	-	0.7349	5.7400	0.6243
DIRECT (Across, Clipped, $\varepsilon = 10.0$ )	0.497	-	0.7665	8.3101	0.7076
DIRECT (Indep, Clipped, $\varepsilon = 10.0$ )	0.596	-	0.7791	8.4024	0.5497
Gemma 1B ( $\varepsilon = 10.0$ )	0.552	-	0.3001	2.6486	0.4454
Gemma 4B ( $\varepsilon = 10.0$ )	0.651	-	0.3784	3.4125	0.3747
Gemini 2.5 FL (0-Shot) ( $\varepsilon = \infty$ )	0.130	-	0.8143	14.5522	1.2082
Gemini 2.5 FL (1-Shot) ( $\varepsilon = \infty$ )	0.265	-	0.7858	5.4584	1.0173
Gemini 2.5 FL (5-Shot) ( $\varepsilon = \infty$ )	0.226	-	0.5023	5.0768	1.0841
Gemini 2.5 FL (10-Shot) ( $\varepsilon = \infty$ )	0.269	-	0.7894	5.9262	1.2283
REAL (10k) ( $\varepsilon = \infty$ )	0.848	-	0.2322	0.3345	0.0161
REAL (1k) ( $\varepsilon = \infty$ )	0.866	-	0.2202	0.7633	0.0430
REAL (100) ( $\varepsilon = \infty$ )	0.866	-	0.1918	1.5563	0.1332

**Table 9 Feature-wise Breakdown of Marginal and Temporal Fidelity (MIMIC-IV).** This table decomposes the aggregate scores into per-feature Wasserstein and Frobenius errors. PATH maintains low transition errors across *all* features. Note that while AIM struggles with transition dynamics generally, it is particularly poor at capturing the stability of ordinal features like pain, where PATH (Gemma 4B) reduces the error by over 50%.

Method	Marginal Distribution (Wasserstein ↓)							State Transition (Frobenius ↓)						
	temp	hear	resp	o2sa	sbp	dbp	pain	temp	hear	resp	o2sa	sbp	dbp	pain
AIM (Clipped, $\varepsilon = 0.5$ )	27.187	16.368	7.145	23.720	28.687	22.992	3.294	0.971	0.918	0.693	1.261	0.855	0.919	0.730
DIRECT (Across, Clipped, $\varepsilon = 0.5$ )	37.486	9.597	2.021	12.354	12.490	15.073	0.669	1.294	0.790	0.522	0.761	0.754	0.826	0.378
DIRECT (Indep, Clipped, $\varepsilon = 0.5$ )	29.550	9.710	2.753	10.727	12.956	19.438	0.501	1.151	0.616	0.611	0.696	0.561	1.114	0.361
Gemma 1B ( $\varepsilon = 0.5$ )	0.669	1.342	12.766	0.523	6.171	4.701	1.362	0.610	0.527	0.506	0.501	0.534	0.449	0.246
Gemma 4B ( $\varepsilon = 0.5$ )	0.860	3.689	1.054	0.852	7.863	4.950	1.750	0.343	0.360	0.282	0.417	0.501	0.480	0.289
AIM (Clipped, $\varepsilon = 2.0$ )	10.531	11.638	3.162	10.536	13.362	18.003	0.723	0.762	0.907	0.458	0.807	0.749	0.907	0.598
DIRECT (Across, Clipped, $\varepsilon = 2.0$ )	23.545	6.687	1.654	7.918	10.209	8.398	1.110	0.905	0.848	0.628	0.506	0.709	0.625	0.615
DIRECT (Indep, Clipped, $\varepsilon = 2.0$ )	24.664	6.938	1.700	6.924	9.868	8.934	1.023	0.875	0.597	0.379	0.673	0.489	0.430	0.505
Gemma 1B ( $\varepsilon = 2.0$ )	0.461	5.498	1.220	0.697	8.195	3.368	0.983	0.403	0.378	0.358	0.273	0.438	0.454	0.239
Gemma 4B ( $\varepsilon = 2.0$ )	0.976	5.987	1.102	0.821	9.248	4.143	0.810	0.414	0.368	0.362	0.405	0.457	0.453	0.247
AIM (Clipped, $\varepsilon = 4.0$ )	9.638	7.611	2.579	6.912	10.767	12.110	0.847	0.572	0.828	0.428	0.509	0.714	0.684	0.598
DIRECT (Across, Clipped, $\varepsilon = 4.0$ )	22.738	7.300	1.796	7.488	10.187	7.386	1.192	0.898	0.837	0.482	0.538	0.705	0.595	0.650
DIRECT (Indep, Clipped, $\varepsilon = 4.0$ )	22.386	6.670	1.775	6.820	10.766	7.107	0.956	0.818	0.572	0.463	0.748	0.496	0.432	0.492
Gemma 1B ( $\varepsilon = 4.0$ )	0.574	6.669	1.125	0.926	8.634	5.065	1.109	0.432	0.369	0.386	0.445	0.461	0.419	0.187
Gemma 4B ( $\varepsilon = 4.0$ )	0.698	7.136	1.198	0.848	8.493	9.324	0.982	0.430	0.354	0.384	0.439	0.454	0.421	0.189
AIM (Clipped, $\varepsilon = 10.0$ )	6.255	7.275	2.019	6.217	9.583	8.037	0.793	0.447	0.814	0.425	0.798	0.703	0.586	0.597
DIRECT (Across, Clipped, $\varepsilon = 10.0$ )	21.799	7.049	1.842	7.825	11.005	7.740	0.911	0.924	0.817	0.490	0.802	0.707	0.600	0.613
DIRECT (Indep, Clipped, $\varepsilon = 10.0$ )	21.276	7.196	1.849	8.859	11.124	7.533	0.979	0.814	0.560	0.373	0.713	0.483	0.405	0.499
Gemma 1B ( $\varepsilon = 10.0$ )	0.765	4.108	1.355	0.453	5.537	4.421	1.902	0.465	0.505	0.509	0.398	0.525	0.474	0.241
Gemma 4B ( $\varepsilon = 10.0$ )	0.546	5.201	1.224	1.946	9.174	4.732	1.064	0.372	0.388	0.366	0.377	0.447	0.455	0.219
Gemini 2.5 FL (0-Shot) ( $\varepsilon = \infty$ )	60.837	10.647	1.288	1.041	14.121	12.641	1.290	1.209	1.416	1.126	1.530	1.338	1.295	0.543
Gemini 2.5 FL (1-Shot) ( $\varepsilon = \infty$ )	0.966	8.754	1.385	1.198	12.342	12.133	1.432	0.911	1.224	0.869	0.904	1.219	1.143	0.851
Gemini 2.5 FL (5-Shot) ( $\varepsilon = \infty$ )	0.531	8.241	1.076	1.469	12.287	10.865	1.069	1.368	0.884	1.257	0.931	1.268	1.056	0.825
Gemini 2.5 FL (10-Shot) ( $\varepsilon = \infty$ )	0.627	10.024	1.393	1.158	12.776	13.755	1.750	1.550	1.342	1.281	1.364	1.097	1.221	0.742
REAL (10k) ( $\varepsilon = \infty$ )	0.062	0.760	0.137	0.060	0.225	1.050	0.048	0.015	0.023	0.005	0.024	0.018	0.018	0.009
REAL (1k) ( $\varepsilon = \infty$ )	0.369	0.894	0.103	0.084	0.488	3.270	0.136	0.075	0.034	0.034	0.055	0.028	0.054	0.021
REAL (100) ( $\varepsilon = \infty$ )	0.205	3.349	0.416	0.315	4.874	1.283	0.452	0.124	0.174	0.117	0.179	0.167	0.129	0.042

**Table 10 Comprehensive Summary of Metrics on Synthetic HMM Data.** This table highlights the utility trade-off between marginal precision and temporal logic. Unsurprisingly, AIM achieves the lowest univariate marginal divergence scores ( $\approx 0.25$  at  $\varepsilon = 4.0$ ). However, AIM’s HMM Likelihood scores remain prohibitively high ( $> 300$ ), indicating the generation of impossible trajectories. We also observe a significant performance gap between Gemma 1B and 4B here that is wider than in the MIMIC experiments; the 1B model struggles to capture the latent HMM states (Likelihood 261.9 vs. 122.8 at  $\varepsilon = 4.0$ ). This is likely because, for the MIMIC and 311 type data, the 1B model has analogous examples from its training data. As this data is fully synthetic with nonsense column names, processing it relies solely on the models reasoning ability coupled with its ability to generalize a prior over tabular data to unseen/unfamiliar domains.

Method	MAUVE (Gecko $\uparrow$ )	HMM Likelihood (Wass. $\downarrow$ )	TDCR (Privacy) (JSD $\downarrow$ )	Marginal Div. (Avg Wass. $\downarrow$ )	State Trans. Div. (Avg Frobenius $\downarrow$ )
AIM ( $\varepsilon = 0.5$ )	0.727	1029.1500	0.8326	2.0781	0.6649
DIRECT (Across, $\varepsilon = 0.5$ )	0.765	1455.6246	0.8326	2.7925	0.7234
DIRECT (Indep, $\varepsilon = 0.5$ )	0.705	1540.8679	0.8268	3.0734	0.7419
Gemma 4B ( $\varepsilon = 0.5$ )	0.237	77.3683	0.2861	1.1648	0.4640
AIM ( $\varepsilon = 2.0$ )	0.655	374.4686	0.6352	0.4260	0.5204
DIRECT (Across, $\varepsilon = 2.0$ )	0.763	696.5508	0.7384	1.5437	0.6014
DIRECT (Indep, $\varepsilon = 2.0$ )	0.701	754.9578	0.8059	1.8809	0.5953
Gemma 1B ( $\varepsilon = 2.0$ )	0.307	334.4557	0.8073	3.0628	1.0329
Gemma 4B ( $\varepsilon = 2.0$ )	0.612	57.9726	0.4150	0.9494	0.4363
AIM ( $\varepsilon = 4.0$ )	0.804	321.6139	0.6262	0.2532	0.4994
DIRECT (Across, $\varepsilon = 4.0$ )	0.802	740.3704	0.7305	0.9890	0.5525
DIRECT (Indep, $\varepsilon = 4.0$ )	0.728	944.7643	0.7624	1.3724	0.5306
Gemma 1B ( $\varepsilon = 4.0$ )	0.268	261.9771	0.6806	2.6619	0.7937
Gemma 4B ( $\varepsilon = 4.0$ )	0.660	122.8850	0.3880	1.0726	0.4670
AIM ( $\varepsilon = 10.0$ )	0.705	319.4292	0.5367	0.2757	0.4791
DIRECT (Across, $\varepsilon = 10.0$ )	0.704	409.1063	0.6560	0.6496	0.5331
DIRECT (Indep, $\varepsilon = 10.0$ )	0.710	653.2374	0.6748	0.9022	0.4558
Gemma 1B ( $\varepsilon = 10.0$ )	0.359	184.9042	0.5402	2.5169	0.7138
Gemma 4B ( $\varepsilon = 10.0$ )	0.690	50.9899	0.3966	0.8250	0.4217
Gemini 2.5 FL (0-Shot) ( $\varepsilon = \infty$ )	0.270	318770.3493	0.8326	53.5924	1.1601
Gemini 2.5 FL (1-Shot) ( $\varepsilon = \infty$ )	0.262	41.8997	0.7800	0.9118	0.7483
Gemini 2.5 FL (5-Shot) ( $\varepsilon = \infty$ )	0.255	96.9679	0.6787	1.0024	0.7310
Gemini 2.5 FL (10-Shot) ( $\varepsilon = \infty$ )	0.268	9.0193	0.5564	0.5596	0.6595
REAL (10k) ( $\varepsilon = \infty$ )	0.856	0.3254	0.1778	0.0325	0.0096
REAL (1k) ( $\varepsilon = \infty$ )	0.892	0.8304	0.1618	0.0517	0.0316
REAL (100) ( $\varepsilon = \infty$ )	0.899	1.5302	0.2069	0.1468	0.0882

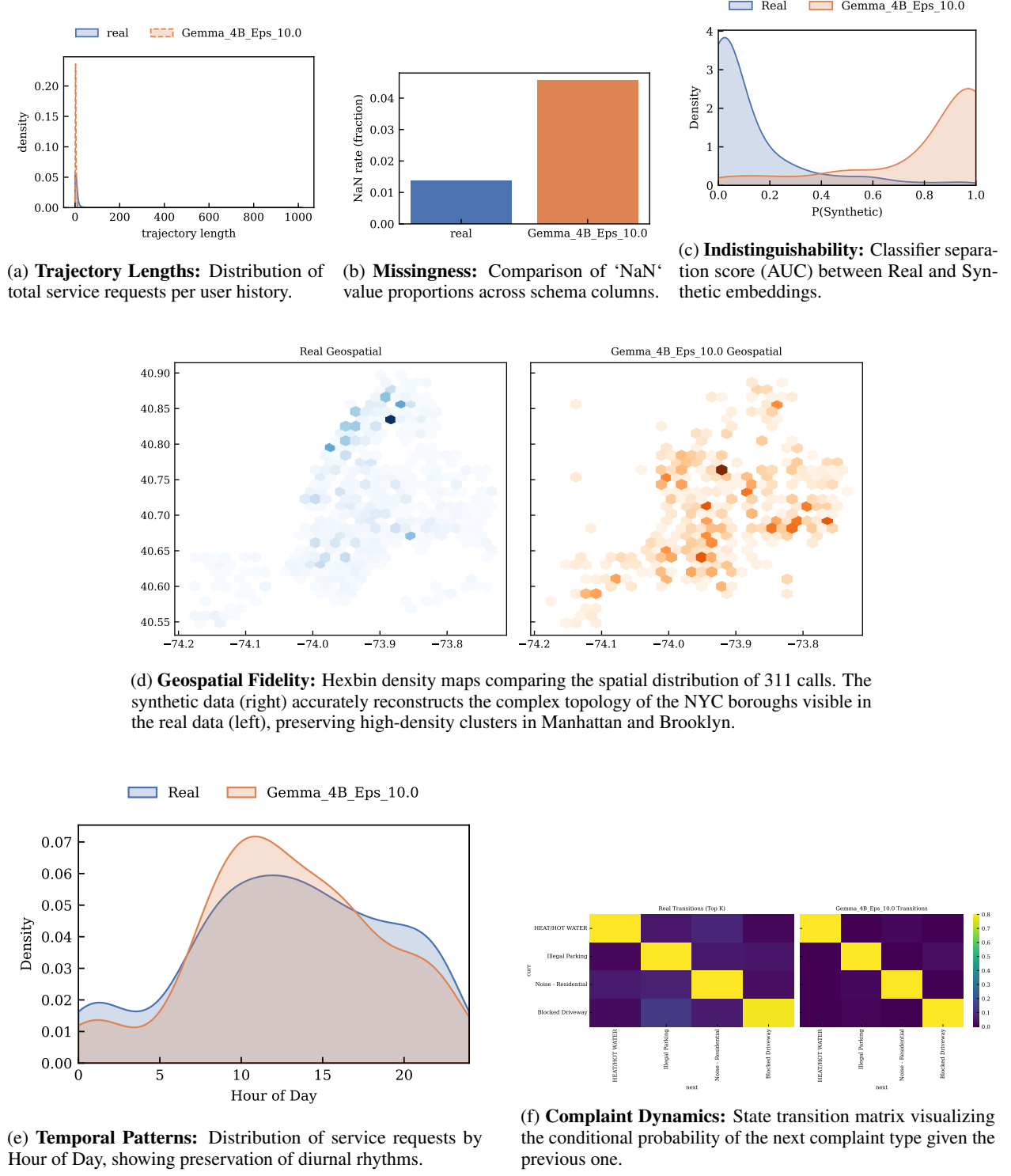
**Table 11 Feature-wise Breakdown on Synthetic Data.** Detailed analysis reveals specific modes of failure for the baselines. For instance, marginal baselines have spiky errors across features; some columns were or were not selected for measurement, and thus the privacy budget is unevenly spread (e.g., DIRECT (Indep) reaches 0.996 at  $\epsilon = 0.5$ , but is then clearly measured at  $\epsilon = 10$ ), while PATH (Gemma 4B) has reasonable results across the board.

Method	Marginal Distribution (Wasserstein $\downarrow$ )					State Transition (Frobenius $\downarrow$ )				
	Glom	Crir	Crip	Zols	Zolp	Glom	Crir	Crip	Zols	Zolp
AIM ( $\epsilon = 0.5$ )	1.325	1.213	1.401	1.443	5.009	0.725	0.662	0.895	0.725	0.318
DIRECT (Across, $\epsilon = 0.5$ )	0.691	0.736	0.863	0.927	10.747	0.640	0.611	0.827	0.638	0.901
DIRECT (Indep, $\epsilon = 0.5$ )	0.742	0.736	0.915	1.042	11.932	0.632	0.596	0.820	0.665	0.996
Gemma 4B ( $\epsilon = 0.5$ )	0.848	0.494	2.593	0.592	1.298	0.586	0.531	0.426	0.325	0.451
AIM ( $\epsilon = 2.0$ )	0.365	0.424	0.374	0.271	0.696	0.600	0.534	0.776	0.531	0.161
DIRECT (Across, $\epsilon = 2.0$ )	0.295	0.399	0.549	0.416	6.060	0.612	0.541	0.790	0.566	0.499
DIRECT (Indep, $\epsilon = 2.0$ )	0.484	0.472	0.580	0.553	7.316	0.583	0.505	0.740	0.533	0.616
Gemma 1B ( $\epsilon = 2.0$ )	3.597	4.102	3.812	1.373	2.429	1.301	1.438	1.064	0.557	0.804
Gemma 4B ( $\epsilon = 2.0$ )	0.913	0.762	0.996	0.570	1.505	0.507	0.447	0.498	0.259	0.471
AIM ( $\epsilon = 4.0$ )	0.261	0.298	0.179	0.147	0.382	0.612	0.530	0.698	0.504	0.153
DIRECT (Across, $\epsilon = 4.0$ )	0.253	0.354	0.392	0.236	3.709	0.607	0.533	0.779	0.546	0.297
DIRECT (Indep, $\epsilon = 4.0$ )	0.378	0.417	0.463	0.350	5.254	0.548	0.481	0.700	0.481	0.443
Gemma 1B ( $\epsilon = 4.0$ )	2.899	3.629	3.238	0.846	2.698	0.568	0.878	1.213	0.577	0.732
Gemma 4B ( $\epsilon = 4.0$ )	0.668	1.176	0.729	0.855	1.935	0.511	0.399	0.588	0.287	0.550
AIM ( $\epsilon = 10.0$ )	0.247	0.327	0.198	0.175	0.432	0.609	0.533	0.614	0.483	0.157
DIRECT (Across, $\epsilon = 10.0$ )	0.212	0.326	0.261	0.246	2.203	0.603	0.532	0.765	0.543	0.221
DIRECT (Indep, $\epsilon = 10.0$ )	0.375	0.415	0.370	0.255	3.096	0.495	0.441	0.628	0.428	0.286
Gemma 1B ( $\epsilon = 10.0$ )	2.763	3.119	3.166	0.610	2.926	0.623	0.724	0.941	0.566	0.715
Gemma 4B ( $\epsilon = 10.0$ )	0.576	0.961	0.660	0.686	1.242	0.528	0.388	0.518	0.284	0.390
Gemini 2.5 FL (0-Shot) ( $\epsilon = \infty$ )	186.225	56.715	16.987	5.976	2.059	1.178	0.996	1.142	1.130	1.354
Gemini 2.5 FL (1-Shot) ( $\epsilon = \infty$ )	0.257	0.494	0.314	0.639	2.855	0.518	0.652	0.596	0.914	1.061
Gemini 2.5 FL (5-Shot) ( $\epsilon = \infty$ )	1.150	0.736	0.445	0.649	2.033	0.942	0.663	0.598	0.576	0.875
Gemini 2.5 FL (10-Shot) ( $\epsilon = \infty$ )	0.526	0.303	0.444	0.284	1.241	0.641	0.488	0.532	0.725	0.912
REAL (10k) ( $\epsilon = \infty$ )	0.028	0.017	0.044	0.025	0.049	0.010	0.007	0.011	0.012	0.008
REAL (1k) ( $\epsilon = \infty$ )	0.063	0.064	0.061	0.020	0.050	0.031	0.035	0.031	0.031	0.030
REAL (100) ( $\epsilon = \infty$ )	0.062	0.087	0.221	0.148	0.216	0.094	0.089	0.081	0.080	0.096

**Table 12 Summary Metrics for NYC 311 Service Requests.** Unlike the tabular MIMIC dataset, the NYC 311 data contains complex, heterogeneous schema elements (geospatial coordinates, categorical descriptors). Here, the disparity between private fine-tuning and non-private prompting is most pronounced: Gemini 3.5 (even with 10-shot) has extremely poor MAUVE scores. PATH (Gemma 4B) demonstrates strong scaling behavior, improving MAUVE from 0.375 to 0.634 as the budget increases from  $\epsilon = 0.5$  to  $\epsilon = 10.0$ . The high Classifier AUC scores across all methods ( $\approx 0.95$ ) show how real 311 requests are hard to perfectly simulate.

Method	MAUVE (Gecko $\uparrow$ )	Classifier AUC (Ideal 0.5)	Temporal Dist. (Wass. $\downarrow$ )	Transition Div. (Frobenius $\downarrow$ )
Gemma 1B ( $\epsilon = 0.5$ )	0.410	0.982	1.922	0.357
Gemma 4B ( $\epsilon = 0.5$ )	0.375	0.952	1.327	0.230
Gemma 1B ( $\epsilon = 2.0$ )	0.353	0.967	1.487	0.239
Gemma 4B ( $\epsilon = 2.0$ )	0.573	0.940	0.823	0.408
Gemma 1B ( $\epsilon = 4.0$ )	0.500	0.951	0.566	0.240
Gemma 4B ( $\epsilon = 4.0$ )	0.566	0.972	1.020	0.295
Gemma 1B ( $\epsilon = 10.0$ )	0.464	0.971	0.870	0.279
Gemma 4B ( $\epsilon = 10.0$ )	0.634	0.948	0.870	0.405
Gemini 3.5 (0-Shot) ( $\epsilon = \infty$ )	0.040	1.000	5.468	-
Gemini 3.5 (1-Shot) ( $\epsilon = \infty$ )	0.062	1.000	4.275	1.927
Gemini 3.5 (5-Shot) ( $\epsilon = \infty$ )	0.056	1.000	2.389	-
Gemini 3.5 (10-Shot) ( $\epsilon = \infty$ )	0.066	1.000	2.131	-
REAL (10k) ( $\epsilon = \infty$ )	0.876	0.470	0.312	0.165
REAL (1k) ( $\epsilon = \infty$ )	0.863	0.529	0.343	0.087
REAL (100) ( $\epsilon = \infty$ )	0.850	0.699	0.881	0.379

### E.1 Detailed Analysis: NYC 311 (Gemma 4B, $\varepsilon = 10.0$ )



(e) **Temporal Patterns:** Distribution of service requests by Hour of Day, showing preservation of diurnal rhythms.

(f) **Complaint Dynamics:** State transition matrix visualizing the conditional probability of the next complaint type given the previous one.

Figure 8: **Qualitative Evaluation on NYC 311 Data (Gemma 4B,  $\varepsilon = 10.0$ ).** The privately fine-tuned model successfully captures multi-modal distributions, including long-tail trajectory lengths (a), complex geospatial densities (d), and daily temporal seasonality (e).

## F.2 Privacy as Regularization

Counter-intuitively, our evaluation of the Synthetic dataset reveals that a larger privacy budget (higher  $\varepsilon$ ) does not necessarily guarantee better distributional matching when measured by e.g. TDCR. The PATH (Gemma 4B) model achieves its lowest (best) Jensen-Shannon Distance (JSD) for the Table-wise Distance to Closest Record (TDCR) metric at the strictest privacy setting of  $\varepsilon = 0.5$ , scoring a JSD of 0.2861. As the privacy budget is relaxed to  $\varepsilon = 2.0$  and  $\varepsilon = 10.0$ , the error surprisingly increases to 0.4150 and 0.3966, respectively. This non-monotonic behavior is confusing.

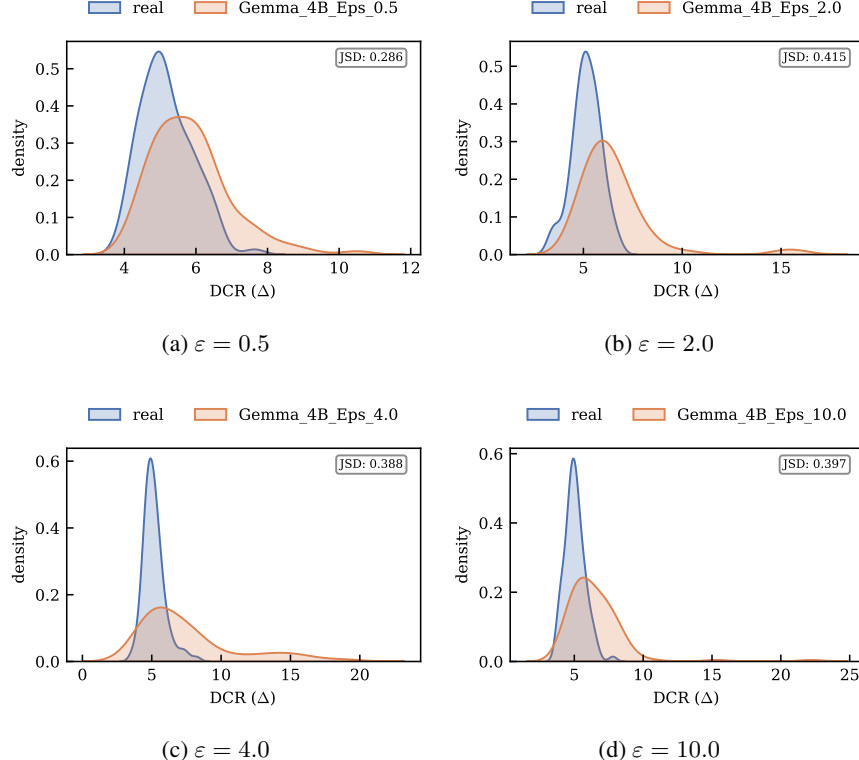


Figure 9: **Evolution of TDCR Density with Privacy Budget.** At low  $\varepsilon$  (0.5), the distribution of distances is tight and well-aligned with the baseline. As  $\varepsilon$  increases (decreasing noise), the model begins to overfit to outliers, creating a heavy tail of generated tables that are topologically distant from the typical data manifold.

We hypothesize that in the high- $\varepsilon$  (low noise) regime, the model retains sufficient capacity to memorize or overfit to outliers and out-of-distribution examples present in the training set. This results in the generation of a “long tail” of synthetic records that drift significantly from the typical data manifold.

This phenomenon is visually evident in Figure 9. At  $\varepsilon = 0.5$  (Figure 9a), the distribution of nearest-neighbor distances is tight; the x-axis extends only to approximately 12, and the curve closely overlaps the reference baseline. However, as we relax the budget to  $\varepsilon = 2.0$  (Figure 9b), a tail begins to emerge, extending the support to 15. By  $\varepsilon = 10.0$  (Figure 9d), the distribution exhibits a long tail.

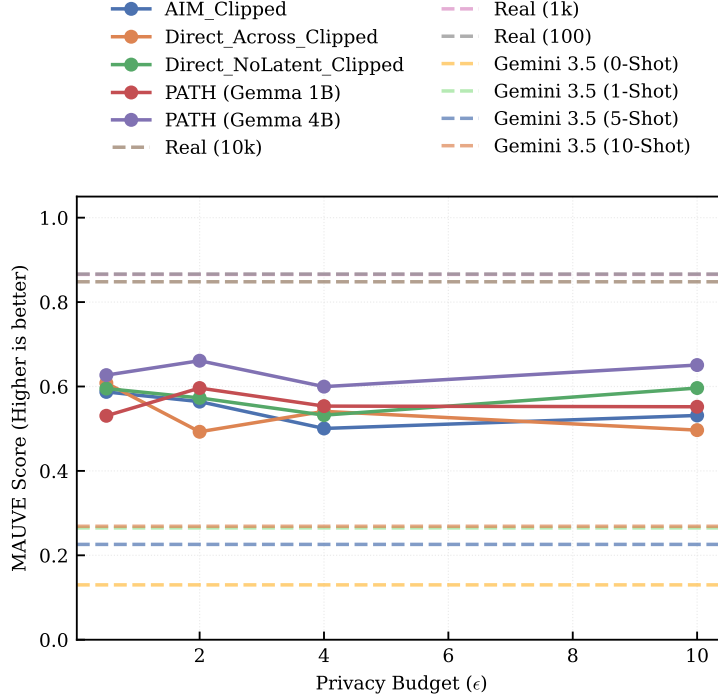


Figure 10: **Distributional fidelity on MIMIC-IV.** The Gemma 4B model (top blue line) consistently achieves the highest MAUVE scores across all privacy budgets, peaking at 0.690 for  $\epsilon = 10$ . Notably, private fine-tuning significantly outperforms the non-private Gemini 2.5 FL baselines (dashed horizontal lines), which fail to exceed 0.30 even with 10-shot prompting. This illustrates that parameter-efficient fine-tuning is far more effective than in-context learning for capturing the complex manifold of clinical trajectories.

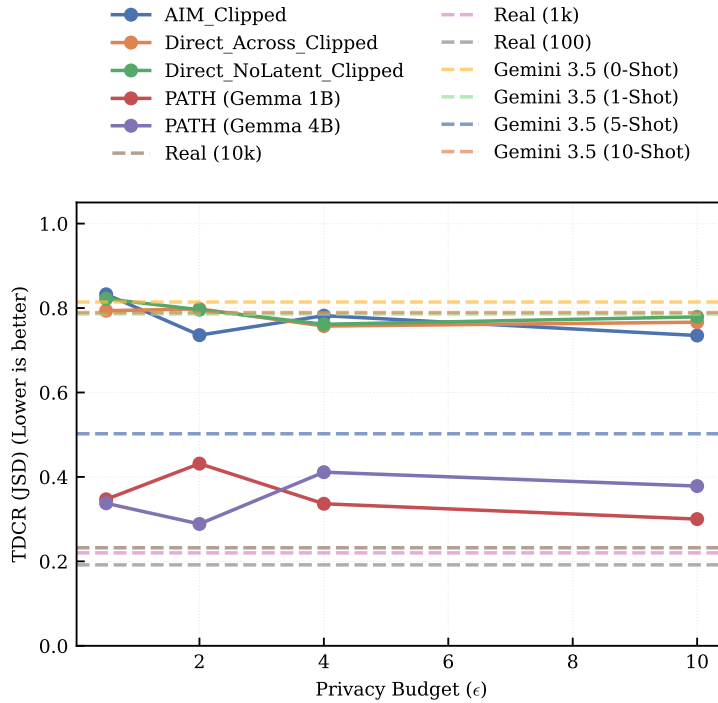


Figure 11: **Distance to closest record analysis.** A lower TDCR score indicates generated tables are structurally similar to real user trajectories without being identical. The marginal-based baselines (AIM and Direct) exhibit high error rates ( $> 14.0$ ) that degrade sharply as  $\epsilon$  decreases, reflecting the failure of “flattening” strategies to model user-level coherence. In contrast, Gemma 4B maintains a low, stable distance ( $\approx 3.9$  to  $7.1$ ) even at  $\epsilon = 0.5$ , demonstrating superior robustness to noise.

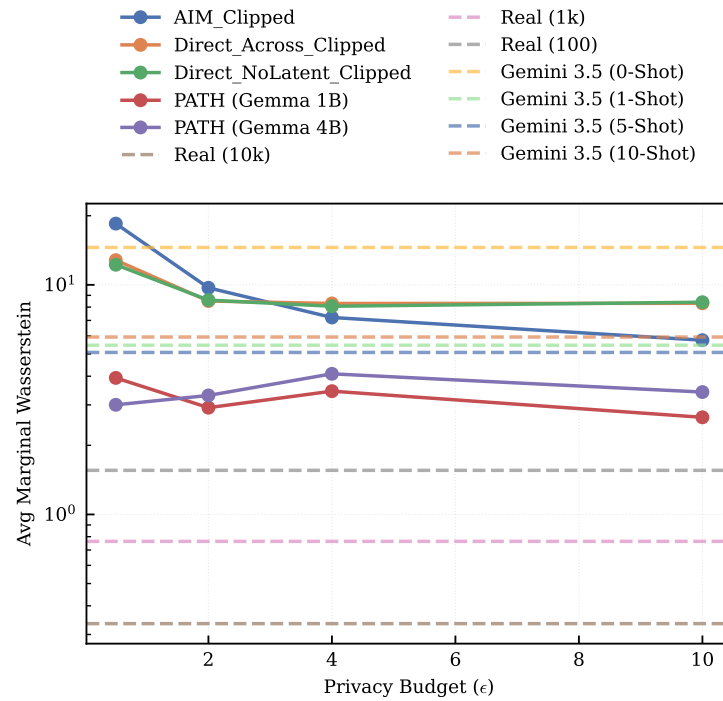


Figure 12: **Preservation of univariate marginals.** Despite being an autoregressive model, Gemma 4B (bottom lines) surprisingly outperforms marginal-based mechanisms on column-wise fidelity, maintaining Wasserstein distances below 4.0 across all budgets. The flattened marginal baselines struggle here, likely due to the high dimensionality introduced by padding all trajectories to a fixed length, which dilutes the privacy budget available for individual column measurements.

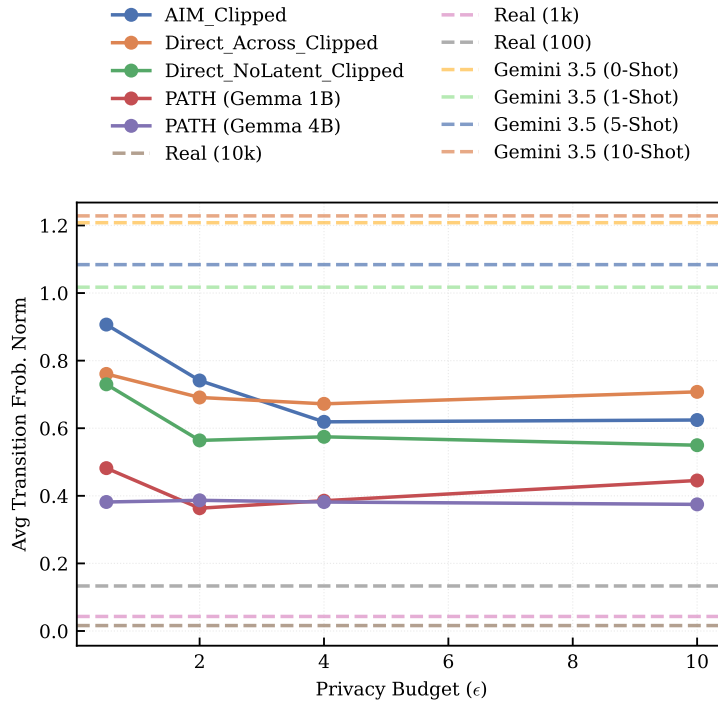


Figure 13: **Temporal dynamics preservation.** This metric measures the error in the conditional probability of state transitions (e.g.,  $P(\text{vital}_t \mid \text{vital}_{t-1})$ ). The Gemma family (1B and 4B) consistently yields lower error rates ( $\approx 0.38 - 0.48$ ) compared to AIM and Direct mechanisms ( $> 0.60$ ). This confirms that the LLM’s autoregressive objective naturally aligns with the task of preserving sequential dependencies, whereas marginal methods struggle to capture these time-variant correlations.

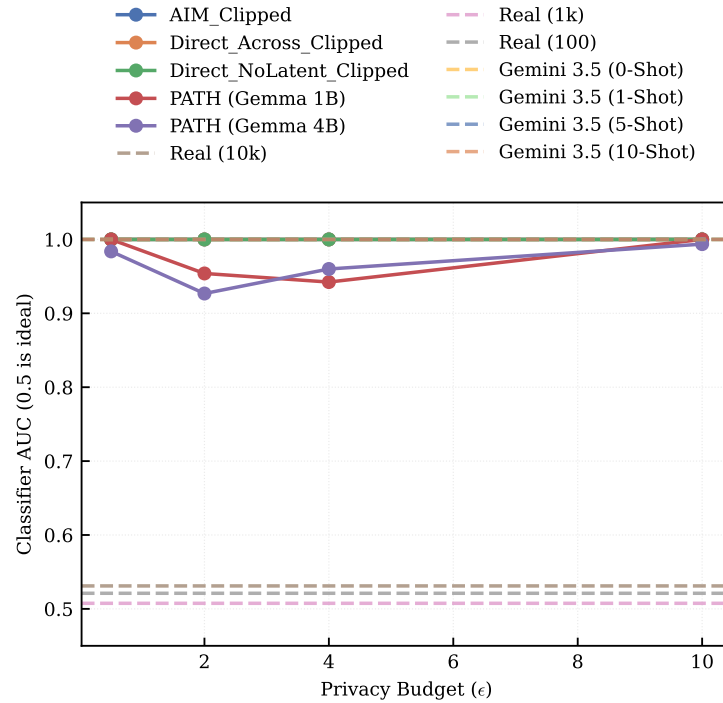


Figure 14: **Discriminability of synthetic data.** While most methods yield an AUC near 1.0 (indicating the synthetic data is distinguishable from real data), the Gemma 1B model shows a slight improvement in indistinguishability at lower privacy budgets (AUC  $\approx 0.95$  at  $\epsilon = 2.0$ ). However, the generally high AUC scores across all methods suggest that while the generated trajectories are statistically useful, they remain distinct enough for a classifier to separate from the original training data.

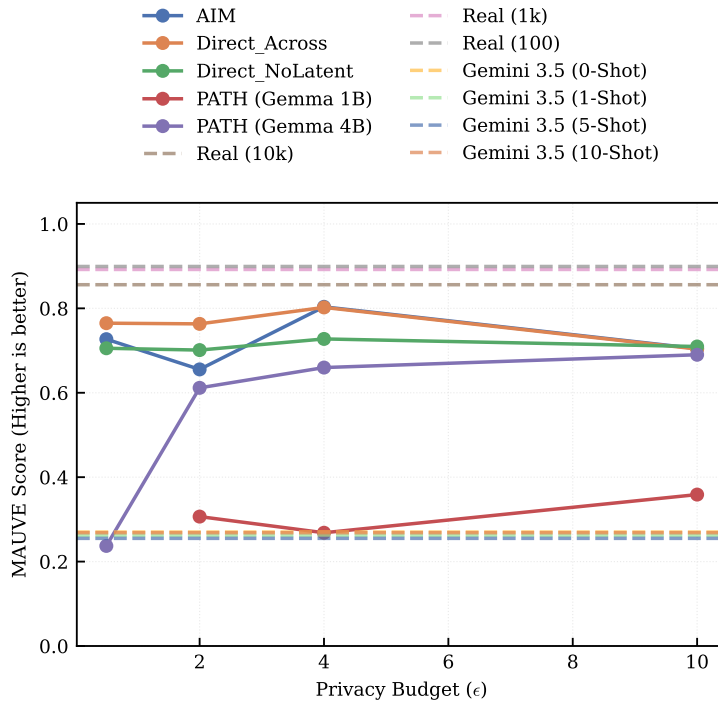


Figure 15: **Distributional fidelity on Synthetic data.** In this controlled setting, the marginal-based AIM algorithm (top lines) outperforms the LLM-based approaches, achieving MAUVE scores between 0.72 and 0.79. This reversal suggests that for simpler, strictly structured data where the manifold is well-defined by independent components, marginal measurements can be more efficient than learning the distribution via next-token prediction.

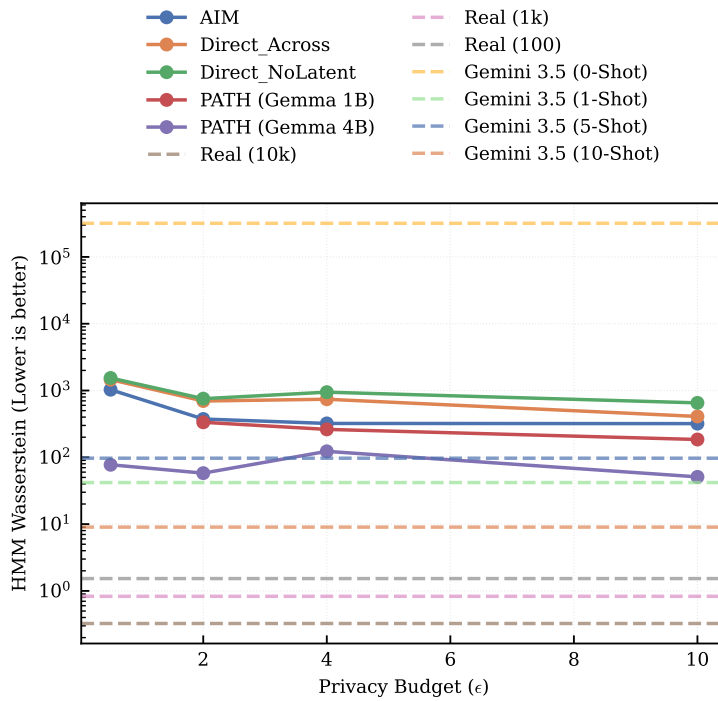


Figure 16: **Likelihood under true latent process.** While AIM captures the static manifold well (see MAUVE), it fails to capture the temporal logic. Gemma 4B achieves significantly lower Wasserstein distances to the true HMM likelihoods ( $\approx 52 - 122$ ) compared to AIM ( $\approx 300 - 1000$ ). This highlights the critical trade-off: marginal methods preserve independent statistics, but autoregressive models are required to preserve the validity of the sequence under the generative process.

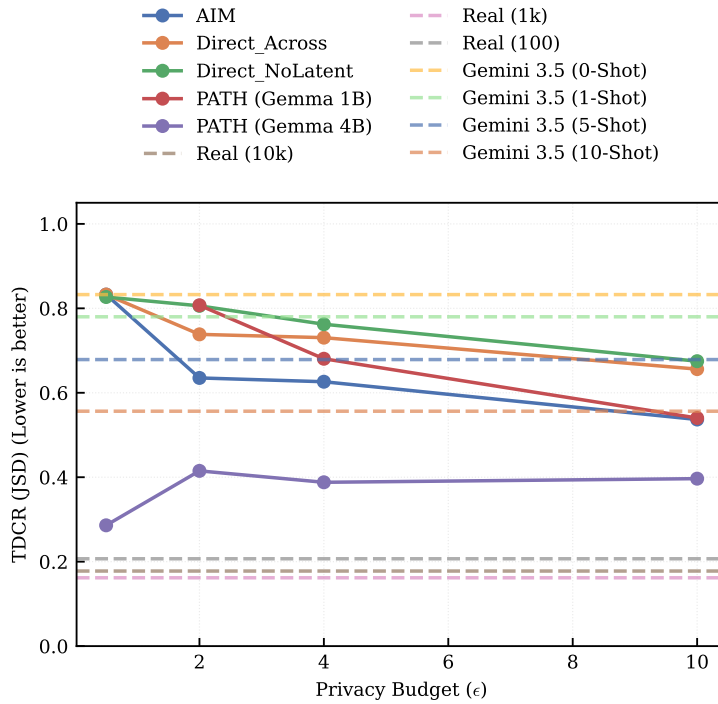


Figure 17: **Structural fidelity on Synthetic data.** Gemma 4B outperforms all baselines with the lowest TDCR scores, particularly at  $\epsilon = 10$  (0.686), indicating it generates trajectories that sit closest to the support of the real data. Notably, the non-private Gemini 2.5 FL 0-shot baseline exhibits a massive error (72.5), further proving that without specific fine-tuning or demonstrations, foundation models cannot zero-shot complex tabular distributions.

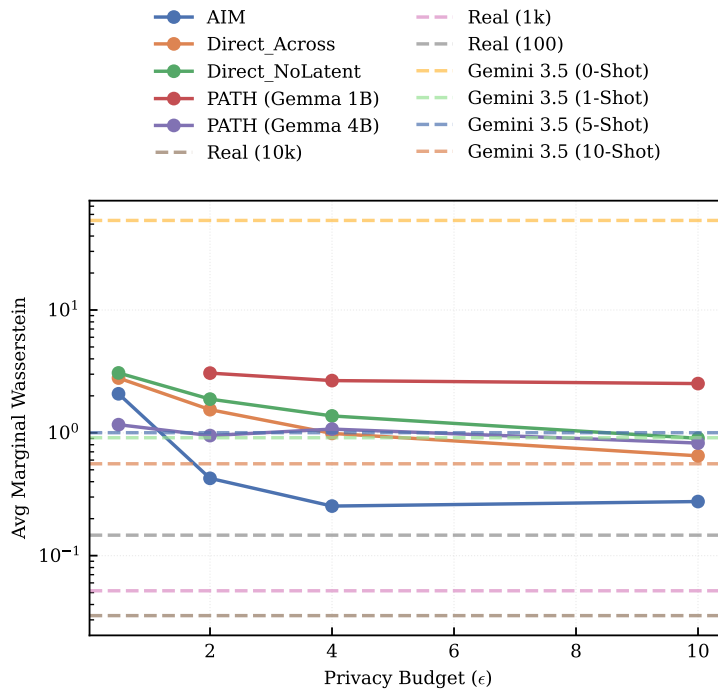


Figure 18: **Column-wise accuracy.** Consistent with the MAUVE results for this dataset, AIM achieves the lowest Marginal Distance ( $\approx 0.23 - 0.26$  for  $\epsilon \geq 4$ ), beating Gemma 4B ( $\approx 0.8 - 1.1$ ). This confirms that when the data generation process is simple and columns have strong independent signals, marginal-based mechanisms utilize the privacy budget more efficiently for univariate statistics.

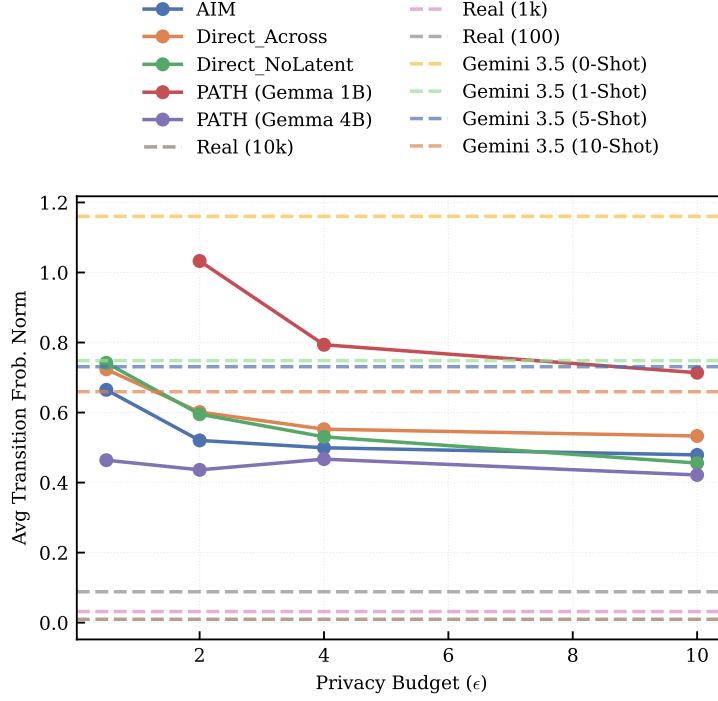


Figure 19: **Transition matrix recovery.** The Gemma 4B model achieves the lowest error in recovering the transition matrix ( $\approx 0.42 - 0.47$ ), slightly outperforming AIM. This reinforces the finding that even when marginal methods excel at static distributions (as seen in the Marginal Distance plot), they are less capable of capturing the derivative, time-dependent structure of the data.

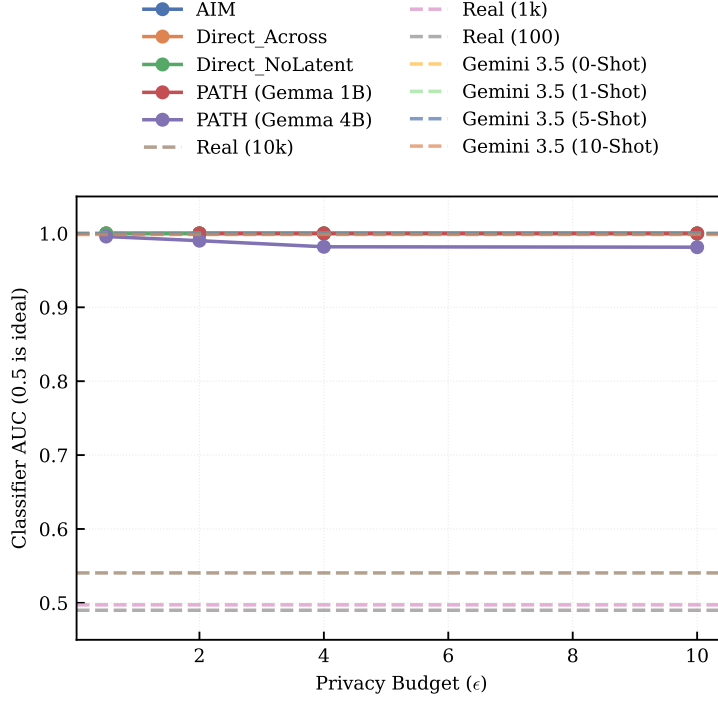


Figure 20: **Discriminability of Synthetic data.**

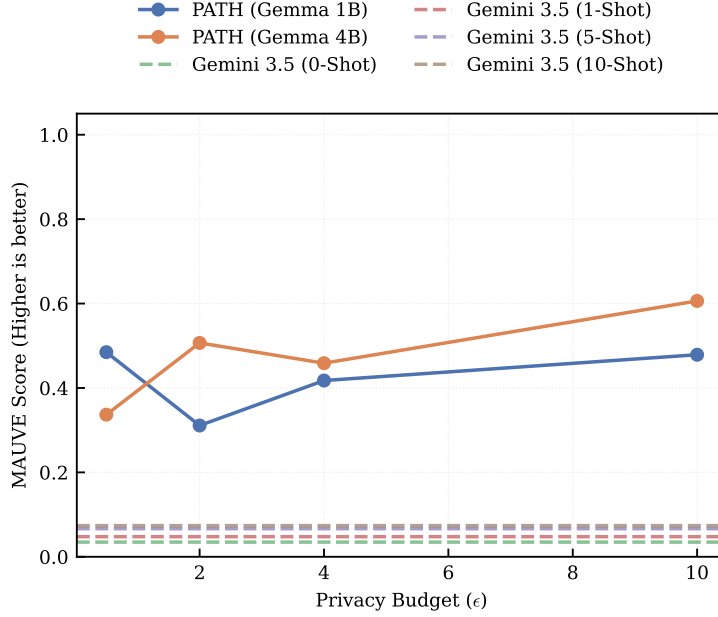


Figure 21: **Fidelity on spatiotemporal data.** The private Gemma models demonstrate a clear advantage on this complex, heterogeneous dataset. Gemma 4B ( $\epsilon = 2.0$ ) achieves a MAUVE score of 0.546, vastly outperforming the non-private Gemini 2.5 FL few-shot baselines, which plateau below 0.10. This indicates that for rich, semantic data like service requests, private fine-tuning is essential for learning the underlying distribution, whereas prompting is insufficient.

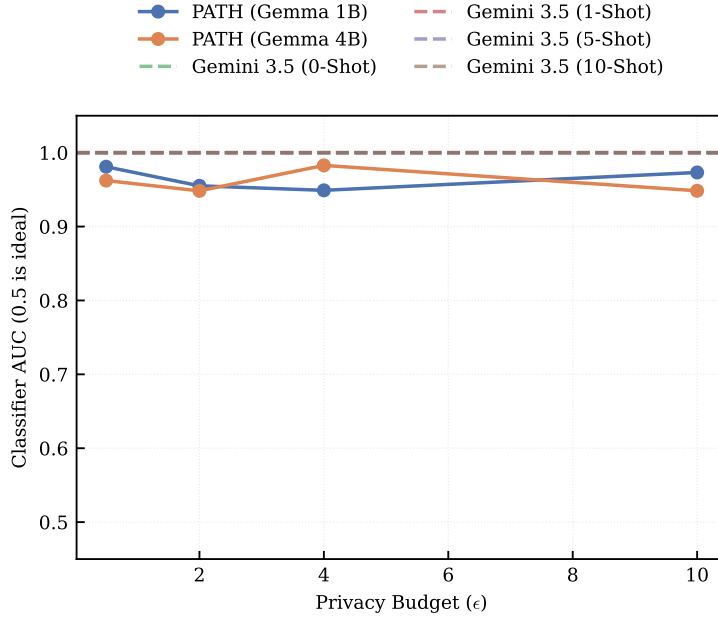


Figure 22: **Discriminability on NYC 311.** Similar to the MIMIC results, the synthetic data remains distinguishable from real data ( $AUC > 0.95$ ). However, the Gemma 1B model shows slightly better resistance to classification than the 4B model at lower epsilons (0.94 at  $\epsilon = 4.0$ ), suggesting a slight regularization effect in the smaller model that prevents it from overfitting to identifiable artifacts.

## G LLM Zero/Few Shot Prompts

### Zero-Shot Prompt Structure

Consider the following domain over patient records (the column names):

<column\_name\_1>, <column\_name\_2>, ..., <column\_name\_n>

Can you now generate a table for another patient, in the same domain as this data?  
Please give me a csv surrounded by “‘csv’ and “‘” tags.

### Few-Shot Prompt Structure (for $k$ examples)

Consider the following set of vital sign time series records, each a single table representing an individual patient (denoted by ‘subject\_id’), where each row is a chart time and set of vitalsign features (with some missingness):

Example Patient 1:

“<CSV String for Patient 1>”

Example Patient 2:

“<CSV String for Patient 2>”

...

Example Patient  $k$ :

“<CSV String for Patient  $k$ >”

Can you now generate a table for another patient, in the same domain as this data?  
Please give me a csv surrounded by “‘csv’ and “‘” tags.

## H Gradient Signal-to-Noise Analysis in High Dimensions

During the fine-tuning of our LLMs with DP-SGD, we observed an interesting phenomenon. Specifically, the  $L_2$ -norm of the noise vector  $\mathbf{z}$  added to the gradients typically exceeded the norm of the true clipped gradient signal  $\bar{\mathbf{g}}$  by several orders of magnitude. Under a standard signal-to-noise Ratio (SNR) interpretation based on raw magnitudes ( $\|\mathbf{g}\|_2 / \|\mathbf{z}\|_2$ ), successful learning appeared unlikely.

However, recent work by Li et al. [18] suggests that  $L_2$ -based SNR is a fundamentally misleading metric for understanding learning dynamics in high-dimensional spaces (in our case,  $d \approx 210$  million trainable parameters for e.g. the 4 billion parameter Gemma model with LoRA). In this section, we present an empirical analysis performed during our experimentation to validate that learning is driven by the *alignment* of the noisy update with a low-dimensional signal subspace, rather than the raw magnitude of the noise.

**Orthogonality and Alignment** Let's build some intuition. Let  $\bar{\mathbf{g}}$  denote the aggregated, clipped gradient computed over a batch, and let  $\mathbf{z} \sim \mathcal{N}(0, \sigma^2 \mathbf{I})$  be the noise vector. The update vector is  $\tilde{\mathbf{g}} = \bar{\mathbf{g}} + \mathbf{z}$ .

In high-dimensional spaces, isotropic Gaussian noise is approximately orthogonal to any fixed low-dimensional subspace with high probability [22]. Assuming the true learning signal lies within a low-dimensional subspace  $\mathcal{S} \subset \mathbb{R}^d$ , the component of the noisy update that drives learning is its projection onto  $\bar{\mathbf{g}}$ . The alignment can be characterized by the dot product, as,

$$\tilde{\mathbf{g}} \cdot \bar{\mathbf{g}} = (\bar{\mathbf{g}} + \mathbf{z}) \cdot \bar{\mathbf{g}} = \|\bar{\mathbf{g}}\|_2^2 + \mathbf{z} \cdot \bar{\mathbf{g}}. \quad (14)$$

Since  $\mathbb{E}[\mathbf{z}] = \mathbf{0}$ , we have  $\mathbb{E}[\mathbf{z} \cdot \bar{\mathbf{g}}] = 0$ . Consequently, in expectation, there is always a positive component of the update in the direction of the signal, provided the optimizer can accumulate this weak signal over many steps without the noise variance causing divergence.

**Some Empirical Metrics** To verify this hypothesis, we consider two metrics during training: expected cosine similarity and the participation ratio.

We measure the alignment between the clean signal  $\bar{\mathbf{g}}$  and the noisy gradient  $\tilde{\mathbf{g}}$ . While the direct cosine similarity is non-linear, we approximate its expectation as,

$$\mathbb{E}[\text{sim}(\bar{\mathbf{g}}, \tilde{\mathbf{g}})] \approx \frac{\|\bar{\mathbf{g}}\|_2}{\mathbb{E}[\|\tilde{\mathbf{g}}\|_2]}. \quad (15)$$

Empirically, we found that while this value is small (on the order of  $10^{-4}$  for  $\sigma = 0.4$ ), it remains consistently positive, confirming that the gradient updates maintain a stable, albeit weak, directional alignment with the loss landscape.

To validate the assumption that the gradient signal is effectively low-rank (sparse in some basis), we compute the participation ratio (PR) [22] of the gradient updates, or,

$$PR(\bar{\mathbf{g}}) = \frac{\left(\sum_{j=1}^d \bar{g}_j^2\right)^2}{\sum_{j=1}^d \bar{g}_j^4} = \frac{\|\bar{\mathbf{g}}\|_2^4}{\|\bar{\mathbf{g}}\|_4^4}. \quad (16)$$

The PR provides a continuous measure of the effective number of active dimensions, ranging from 1 (maximal localization) to  $d$  (maximal delocalization).

**Observations** We compared training runs with a standard noise multiplier ( $\sigma = 0.4$ , corresponding to  $\varepsilon \approx 10$ ) against ablations with high noise ( $\sigma = 10.0$ ).

As shown in Figure 24, we observed  $PR(\bar{\mathbf{g}}) \ll d$  (typically orders of magnitude lower than the parameter count  $2.1 \times 10^8$ ), providing strong evidence that the gradients occupy a low-dimensional manifold. This sparsity allows DP-SGD to navigate the optimization landscape despite the overwhelming ambient noise.

Conversely, at  $\sigma = 10.0$ , we reach a critical threshold  $\sigma_{\text{crit}}$  where the utility bound becomes vacuous, and the alignment (Figure 23b) becomes dominated by stochastic variance, preventing effective learning. These findings validate the theoretical bounds proposed by Song et al. [34], Li et al. [18] and justify our choice of hyperparameters.

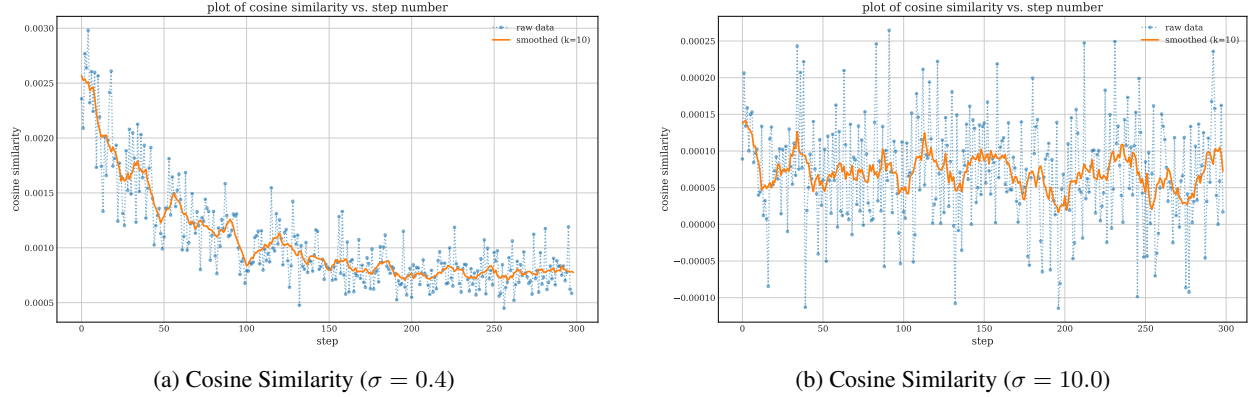


Figure 23: Cosine similarity between the signal and the noisy gradient. At operational noise levels (Left), a consistent positive alignment is observed. At critical noise levels (Right), alignment degrades significantly.

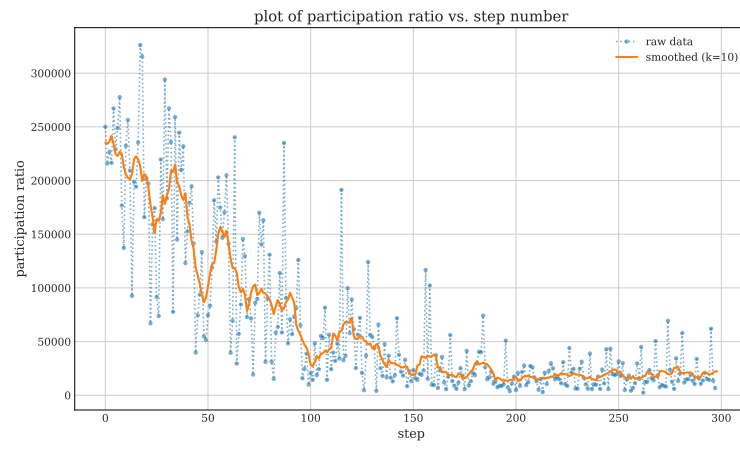


Figure 24: The Participation Ratio (PR) of the gradients (log scale) during training. The PR remains orders of magnitude below the ambient dimension  $d$ , indicating the effective gradients are confined to a low-dimensional subspace.